Marked Consequences of Systematic Oligothiophene Catenation in Thieno[3,4-c]pyrrole-4,6-dione and Bithiopheneimide Photovoltaic Copolymers

Nanjia Zhou,[†] Xugang Guo,*,[‡,§] Rocio Ponce Ortiz,*,[∥] Tobias Harschneck,[‡] Eric F. Manley,[‡,⊥] Sylvia J. Lou,[‡] Patrick E. Hartnett,[‡] Xinge Yu,[‡] Noah E. Horwitz,[‡] Paula Mayorga Burrezo,[∥] Thomas J. Aldrich,[‡] Juan T. López Navarrete,[∥] Michael R. Wasielewski,*,[‡] Lin X. Chen,*,[‡,⊥] Robert. P. H. Chang,*,[†] Antonio Facchetti,*,[‡,#] and Tobin J. Marks*,[†,‡]

[†]Department of Materials Science and Engineering and the Materials Research Center, the Argonne-Northwestern Solar Energy Research Center, Northwestern University, 2145 Sheridan Road, Evanston, Illinois 60208, United States

[‡]Department of Chemistry and the Materials Research Center, the Argonne-Northwestern Solar Energy Research Center, Northwestern University, 2145 Sheridan Road, Evanston, Illinois 60208, United States

[§]Department of Materials Science and Engineering, South University of Science and Technology of China, No. 1088, Xueyuan Boulevard, Shenzhen, Guangdong 518055, China

[∥]Department of Physical Chemistry, University of Málaga, Campus de Teatinos s/n, Málaga 29071, Spain

[⊥]Chemical Sciences and Engineering Division, Argonne National Laboratory, 9700 South Cass Avenue, Lemont, Illinois 60439, United States

[#]Polyera Corporation, 8045 Lamon Avenue, Skokie, Illinois 60077, United States

S *Supporting Information*

ABSTRACT: As effective building blocks for high-mobility transistor polymers, oligothiophenes are receiving attention for polymer solar cells (PSCs) because the resulting polymers can effectively suppress charge recombination. Here we investigate two series of in-chain donor−acceptor copolymers, **PTPDnT** and **PBTInT**, based on thieno[3,4-c]pyrrole-4,6-dione (**TPD**) or bithiopheneimide (**BTI**) as electron acceptor units, respectively, and oligothiophenes (**nTs**) as donor counits, for high-performance PSCs. Intramolecular S···O interaction leads to more planar **TPD** polymer backbones, however backbone torsion yields greater open-circuit voltages for **BTI** polymers. Thiophene addition progressively raises polymer HOMOs but marginally affects their band gaps. FT-Raman spectra indicate that **PTPDnT** and **PBTInT** conjugation lengths scale with **nT** catenation up to n = 3 and then saturate for longer oligomer. Furthermore, the effects of oligothiophene alkylation position are explored, revealing that the alkylation pattern greatly affects film morphology and PSC performance. The **3T** with "outward" alkylation in **PTPD3T** and **PBTI3T** affords optimal π-conjugation, close stacking, long-range order, and high hole mobilities (0.1 cm²/(V s)). These characteristics contribute to the exceptional ~80% fill factors for **PTPD3T**-based PSCs with PCE = 7.7%. The results demonstrate that **3T** is the optimal donor unit among **nTs** (n = 1−4) for photovoltaic polymers. Grazing incidence wide-angle X-ray scattering, transmission electron microscopy, and time-resolved microwave conductivity measurements reveal that the terthiophene-based **PTPD3T** blend maintains high crystallinity with appreciable local mobility and long charge carrier lifetime. These results provide fundamental materials structure-device performance correlations and suggest guidelines for designing oligothiophene-based polymers with optimal thiophene catenation and appropriate alkylation pattern to maximize PSC performance.
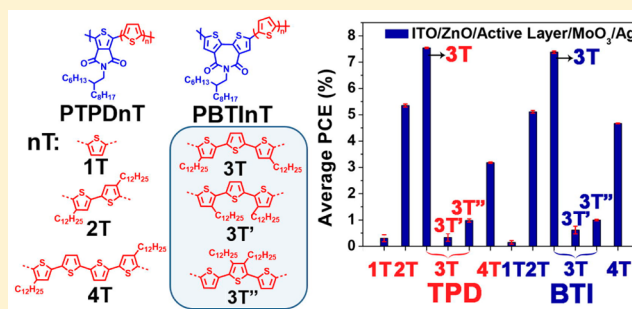
INTRODUCTION

Impressive advances have been achieved over the past two decades in polymer-based optoelectronic devices such as organic thin-film transistors (OTFTs) and polymer solar cells (PSCs) which, as emerging technologies, could complement/replace current inorganic materials-based devices by being mechanically flexible, less costly, suitable for roll-to-roll processing, and lightweight.[1−5] In the PSC arena, research progress has been made predominantly in bulk-heterojunction (BHJ) blends where the photoactive layer consists of interpenetrating hole-transporting/electron-donating and electron-transporting/electron-accepting networks.[6−8] Combined advances in materials synthesis/characterization, computation/simulation, and device engineering

Scheme 1. Chemical Structures of High-Performance Organic Semiconductors Containing Oligothiophene Building Blocks[a]
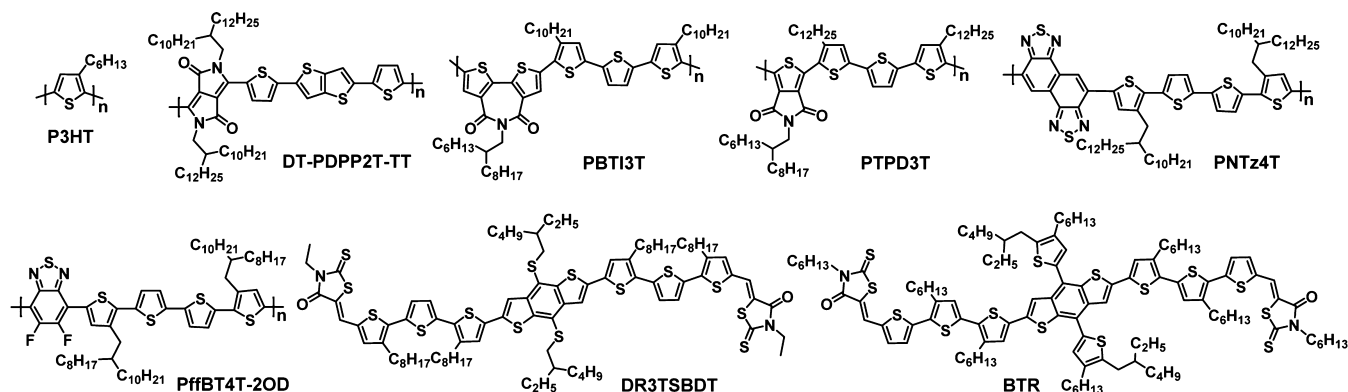
[a]These materials demonstrate the highest fill factors (74–80%) and state-of-the-art power conversion efficiencies (7–11%) to date in organic (small molecule and polymer) solar cells.

have afforded much improved PSC performance. So far, the binary BHJ blends of polymer donors and the [6,6]-phenyl-C_{71}-butyric acid methyl ester (PC$_{71}$BM) acceptor have provided remarkable single-junction power conversion efficiencies (PCEs) as high as ~9–11%,[9–11] forecasting a promising future for PSCs.

Numerous computational and experimental results suggest the importance of materials electronic properties and orbital energetics for PSC materials design, with key requirements being sufficient energetic offset between the lowest unoccupied molecular orbitals (LUMOs) of donor and acceptor materials for exciton splitting, lowering the highest occupied molecular orbital (HOMO) of the donor to enlarge the open-circuit voltage (V_{oc}) and environmental stability,[12–15] and compressing the optical band gap for greater light capture and higher short-circuit currents (J_{sc}'s).[16–18] To this end, design strategies based on copolymerization of an electron-rich donor (D) with an electron-deficient acceptor (A) are widely employed to precisely tune HOMO and LUMO energetics as well as band gaps of the resulting polymers.[19] To achieve this goal, tuning the in-chain charge transfer character between donor and acceptor blocks of copolymers plays pivotal roles. In fact, the rapid PSC performance advances over the past decade reflect the successful design and synthesis of effective building blocks and their incorporation into polymers.[20–25] Among possible acceptor units, imide-functionalized arenes have attracted attention and have achieved great success for constructing high-performance polymers, owing to several distinctive characteristics:[23,26] (i) the strong imide electron-withdrawing properties offer broad-range manipulation of frontier MOs (FMOs) and band gaps; (ii) the planar polymer backbones facilitate efficient intermolecular/interchain charge transport; (iii) high polymer molecular weight is favored by Stille coupling.[23,27] Indeed, polymers containing thieno[3,4-c]pyrrole-4,6-dione (**TPD**) and bithiopheneimide (**BTI**) have recently provided remarkable OTFT and PSC performance.[26,28–32] For example, with **TPD** and **BTI** units as the acceptors, p-type mobilities of 0.6–1.3 cm^2/(V s) and PCEs of 7–9% were demonstrated in OTFTs and PSCs, respectively.[6,33–35]

Among possible in-chain electron donors, benzodithiophene,[21,22] naphthodithiophene,[36] and dithienosilole/germole[26,34,37] have recently played key roles in maximizing PCEs. However, despite this success, polymers composed of the above units typically exhibit low degrees of long-range order and modest mobilities. Note also that significant order and mobility are essential for suppressing charge recombination and enhancing charge extraction in disordered PSC BHJ films.[38] In the OTFT arena,

oligothiophenes (**nTs**) have been widely employed for constructing high mobility polymers,[39–41] while their application in PSCs has been relatively sparse. **nTs** typically have a high degree of conjugation due to the small thiophene resonance energy, which should enhance solar absorption when copolymerized with appropriate acceptor co-units. Furthermore, the large mobilities of **nT**-based polymers may suppress charge recombination and thus enhance the fill factor (FF) and short-circuit current (J_{sc}). In our first report of FF enhancement as an approach to highly efficient PSCs, we employed high-mobility terthiophene (**3T**)-based polymers.[35] Although such polymers, **PTPD3T** and **PBTI3T** (Scheme 1), have moderate band gaps (~1.8 eV), the resulting PSCs provide high PCEs of ~8.7%, which is primarily attributed to the exceptional FFs (~80%).[35] In the literature, polymers having the most promising FFs (>74%) are almost invariably constructed from **nTs** (**P3HT**, **PNTz4T**, and **PffBT4T-2OD**, Scheme 1) or fused thiophenes (**DT-PDPP2T-TT**).[11,35,42–45] When other parameters are optimized, such as the band gap and HOMO, the highest PCE of 10.8% is achieved from a benzothiadiazole-tetrathiophene copolymer (**PffBT4T-2OD**).[45] **nTs** have also shown great potential in small molecule solar cells (**DR3TSBDT** and **BTR**) with high PCEs (>10%)[46] and FFs (74–77%).[47,48] These results argue that oligothiophenes (**nTs**) are promising building blocks for designing new organic semiconductors for solar cell applications.

Excepting HOMO/LUMO energetics, many fundamental questions about PSC polymer design remain unanswered, which surely play significant roles in cell performance.[49] Solid state polymer–polymer interactions and polymer–fullerene nano-/microstructural assembly strongly influence charge transport and optoelectronic processes in multiple, incompletely understood ways.[50–53] Moreover, the blend film morphology, degree of crystallinity, donor–acceptor phase separation, and domain sizes are strongly dependent on complex polymer–fullerene interactions. Nevertheless, empirical fine-tuning of noncovalent intermolecular interactions, especially via optimized in-chain D–A arrangement and backbone substitution, when successful, are remarkably effective in controlling polymer self-assembly, hence promoting long-range order for charge transport over macroscopic device length scales.[54,55]

Motivated by the emerging significance of oligothiophenes in high-performance polymer semiconductors, and by established fundamental polymer structure-PSC response relationships, here we systematically investigate the role of oligothiophene catenation—monothiophene (**1T**), bithiophene (**2T**), terthiophene

Scheme 2. Chemical Structures of Copolymers Based on TPD or BTI Acceptor Units and Various Oligothiophenes As Donor Co-units[b]
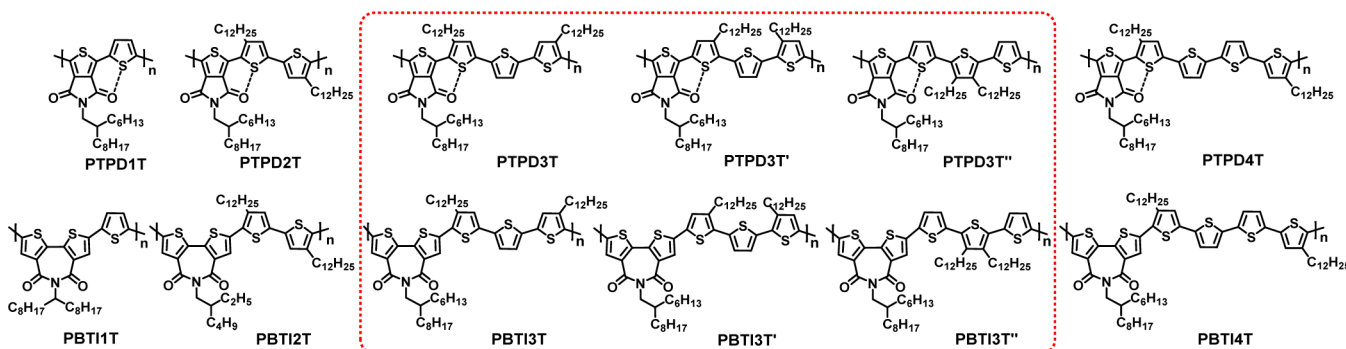
[b]The terthiophene-based polymers having different alkylation patterns are shown in the red square, and the intramolecular (thienyl)S···O(carbonyl) interactions in **TPD** polymers are indicated by dashed lines.

Table 1. Molecular Weight and Optical Property Data for the Polymer Series PTPDnT and PBTInT

Polymer	M_n (kDa)/PDI[a]	λ_{max} sol (nm)[b]	$\lambda_{shoulder}$ sol (nm)[b]	λ_{max} film (nm)[c]	$\lambda_{shoulder}$ film (nm)[c]	λ_{onset} film (nm)	E_g^{opt} (eV)[d]
PTPD1T	4.8/2.2	570	612, 650	636	584	717	1.73
PTPD2T	17.3/1.4	471	625	575	617	681	1.82
PTPD3T	40.0/2.5	585	628	582	628	681	1.82
PTPD3T′	10.5/2.0	515		525	623	681	1.82
PTPD3T″	20.7/1.9	523	611	569	530, 615	681	1.82
PTPD4T	9.4/1.8	512	577, 629	630	537, 578	678	1.83
PBTI1T	5.2/1.8	546	602	602	561	669	1.85
PBTI2T	10.8/2.9	502	571, 631	573	533, 620	683	1.82
PBTI3T	27.4/2.7	595	634	624	582	681	1.82
PBTI3T′	32.8/2.8	637	589	630	582	681	1.82
PBTI3T″	34.1/1.8	560	607	567	602	674	1.84
PBTI4T	15.8/2.4	578	537, 635	628	541, 579	680	1.82

[a]GPC versus polystyrene standards, trichlorobenzene as eluent, at 150 °C. [b]Solution absorption spectra (1×10^{-5} M in chloroform). [c]Thin film absorption spectra from pristine film cast from 5 mg/mL chloroform solution. [d]Optical band gap estimated from absorption edge of the as-cast thin film.

(**3T**), tetrathiophene (**4T**)—and spacing between donor co-unit solubilizing substituents. Additionally, to further probe structure–property relationships and elucidate nonenergetic effects on the performance of polymers derived from the best-performing **PTPD3T** and **PBTI3T** where the alkyl chains are directed "outward", we now study their isomers where the *n*-dodecyl chains are directed "inward" (**PTPD3T′** and **PBTI3T′**) and are installed on the central thiophene β-positions (**PTPD3T″** and **PBTI3T″**). Scheme 2 shows the **TPD** and **BTI** copolymers, employing **1T**−**4T** as the donor co-units. On both **TPD** and **BTI** units, branched 2-hexyldecyl chains are installed for most of the polymers. Except for **PTPD1T** and **PBTI1T** which do not have solubilizing chains on monothiophenes, all other polymers have the same *n*-dodecyl chains on donor co-units for better comparison. It will be seen that these chain combinations impart sufficient solubility for device fabrication. Although some of these **nT**-based copolymers containing **TPD**[35,56,57] and **BTI**[35] have been reported previously, and **nT**s have been copolymerized with acceptors such as diketopyrrolopyrrole,[23,58] isoindigo,[23,59] and benzothiadiazole,[11,60] there has been no systematic investigation of **nT** extension and side chain position effects on PSC properties. Here we present such a study, employing optical absorption spectroscopy, Raman spectroscopy, transmission electron microscopy (TEM), grazing incidence wide-angle X-ray scattering (GIWAXS), organic thin-film transistor (OTFT) mobility, space-charge limited current (SCLC) mobility, and time-resolved microwave conductivity (TRMC) measurements, to probe the effects of

nT catenation and alkylation positioning in achieving high charge mobility and optimal blend film morphology. We show this can lead to favorable energy level alignment, improved charge extraction, reduced bimolecular recombination, high fill factor, and hence enhanced PCE. The findings offer useful insights for designing more efficient PSCs using oligothiophene structures.

■ RESULTS AND DISCUSSION

Materials Synthesis. Detailed synthetic information for monomers and polymers is reported in the Supporting Information (SI). Before polymerization, the monomers were subjected to rigorous purification to achieve sufficient purity. All polymers were synthesized via Pd-mediated Stille coupling in toluene at 110 °C. After polymerizations, polymer chains were end-capped with monofunctionalized thiophene. The resulting purple-blue polymers were then subjected to purifications via Soxhlet extractions using a different solvent sequence, depending on polymer solubility. The identity and purity of the resulting polymers were supported by high-temperature (100−130 °C) ^{1}H NMR as well as elemental analysis. Polymer molecular weights were measured by high-temperature (150 °C) gel permeation chromatograhy (GPC) vs polystyrene standards using trichlorobenzene as eluent. All polymers afford sufficient solubility for device fabrication in common organic solvents. Number-average molecular weight (M_n), and polydispersity index (PDI) data are summarized in Table 1. Due to the low solubility, polymers **PTPD1T** and **PBTI1T** precipitated at the early stage of
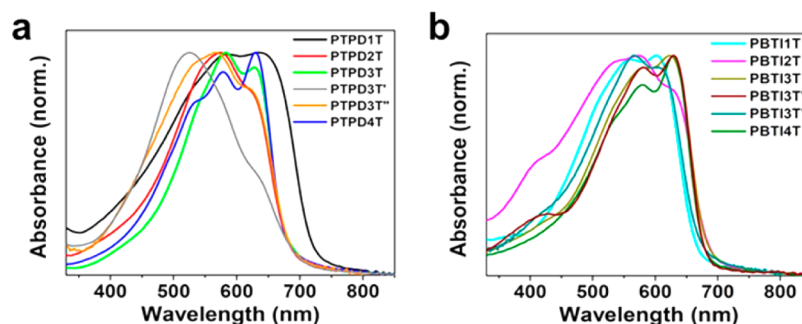
Figure 1. Optical absorption spectra of **PTPDnT** series (a) and of **PBTInT** series (b) as thin films spun cast from chloroform (5 mg/mL).

polymerization, and the soluble portion only shows low M_n (~5 kDa). Among all polymers, the polymerization of **PTPD3T** is most effective, and the resulting polymer can achieve M_n as high as ~40 kDa. Therefore, the **PTPD3T** having various M_n was synthesized by controlling monomer stoichiometry ratios.

Optical Spectra. Figure 1 shows the absorption spectra of all polymer films, and the relevant data are summarized in Table 1. On the basis of these spectra, systematic trends in spectral features as a function of **nT** size are not obvious. The most noticeable feature is the **PTPD1T** absorption in the reddest region with a spectral onset of >700 nm, which is likely connected to its fully conformationally locked polymer backbone enabled by the consecutive S···O interactions. However, the S···O interactions are absent in **BTI** polymers,[26,35] while other **TPD** polymers with more extended **nT** lack such consecutive interactions because of the presence of the bithiophene subunit in **nT**. Hence, both series of polymers have comparable optical band gaps of 1.82−1.85 eV, except for **PTPD1T**, indicating that thiophene catenation and varying side chain positions negligibly influence the band gap. In the solid state, excepting **PTPD3T′**, all polymers have an absorption maximum accompanied by a distinctive shoulder, indicating a substantial degree of backbone coplanarity. Another distinctive feature in this study is the absorption of **PTPD3T′**, which is discussed below.

In comparison to analogues having more extended **nT** units, the **2T** polymers show substantially blue-shifted absorption maxima in solution (Figure S1). Among all polymers, **2T**-based polymers **PBTI2T** and **PTPD2T**, especially **PTPD2T**, lack vibronic features in the principal absorption peak, suggesting structural heterogeneity in solution, presumably due to the nonplanar conformational disorder imposed by the side chains. The blue-shift of the **2T**-based polymers likely originates from reduced backbone coplanarity due to the high alkylation density, which creates interchain repulsions and suppresses aggregation in solution. With the insertion of additional thiophenes, **PTPD3T** and **PTDD4T** compared to **PTPD2T** exhibit red-shifted absorptions, suggesting a higher degree of π-delocalization and solution phase aggregation. Similar absorption feature trends as a function of thiophene catenation are also observed in the **PBTI** series. However, the difference in this series is that **BTI** is far bulkier than **TPD** with a stronger tendency to aggregate. From comparison of the solution absorption profiles of **PBTI2T** and **PTPD2T**, **PBTI2T** shows red-shifted absorption with some vibronic features, and the low energy region is more intense for **PBTI2T** than for **PTPD2T**. The stronger **PBTI2T** aggregation is favored by the fused bithiopheneimide unit in **PBTI2T**, which is the dominant solution phase factor in the **BTI**-based polymers versus the S···O interaction in the **TPD**-based polymers. However, in the film state, the intramolecular

S···O interaction in **TPD** polymers becomes more important, which leads to higher crystallinity for **TPD** polymers in the film state.

Focusing on the **3T** isomers, side chain regiochemistry has distinctive effects on polymer optical properties, with **PTPD3T′** and **PTPD3T″** both exhibiting blue-shifted film absorption maxima (525 and 569 nm, respectively) versus **PTPD3T** (582 nm), indicating the reduced **PTPD3T′** and **PTPD3T″** backbone planarity (see more below). Note that steric hindrance is significantly reduced in **PTPD3T** due to the increased space between side chains and the opposite side chain orientations, however significant steric hindrance persists in **PTPD3T′** and **PTPD3T″**. Such local conformational differences account for the monotonic blue-shifted main absorption trends in **PTPD3T′** and **PTPD3T″** versus **PTPD3T** which exhibits red-shifted maxima with vibronic features. The "inward" alkylation pattern in **PTPD3T′** creates significant steric hindrace, leading to the most blue-shifted absorption, the greatest lamellar stacking distance (40.7 Å), the lowest mobilities (10^{-6} cm²/(V s)), and the poorest PCE (0.34%), *vide infra*. For the larger **BTI**-based **3T** isomer, **PBTI3T″** also shows significantly blue-shifted film absorption maxima (567 nm) in film versus that (624 nm) of **PBTI3T**, while the absorption profile of **PBTI3T′** is similar to that of **PBTI3T**. In comparison to **TPD**, the expanded **BTI** core in **PBTI3T′** mitigates the steric hindrance in contrast to **PTPD3T′**, which exhibits the most blue-shifted absorption. Hence, the polymer conjugation is sensitive to not only the alkylation pattern, but also the spacing between the alkyl chains and/or the acceptor dimensions.[33,59,61]

Molecular Geometry and Frontier Molecular Orbital Computation. Figure 2 shows top and side views of energy-minimized molecular models for **PTPDnT** and **PBTInT** computed by DFT. For the **PTPDnT** series, the dihedral angle between **TPD** and **nT** moieties in the repeat unit are found to be only −1° to −3°, suggesting strict coplanarity stabilized by the intramolecular (thienyl)S···O(carbonyl) interactions.[54,62] Interestingly, for **PBTInT** series, the dihedral angles between **BTI** and **nT** planes are significantly larger (−12° to −14°), implying greater backbone torsion versus the **TPD** counterparts. This result is consistent with previous studies where it was proposed that the larger **BTI** core prevents close S···O contacts.[26] Thus, with all other factors being equal, the **PTPDnT** polymers are expected to have greater crystallinity and long-range order. To better understand the effects of alkylation regiochemistry on the **3T** polymer geometries and orbital energies, energy-minimized molecular geometries were computed by DFT for the **3T**-based copolymer models (Figure 3). Note that skeletal planarity is diminished upon changing from "outward" alkyl substitution in **PTPD3T** to "inward" substitution in two nonconsecutive
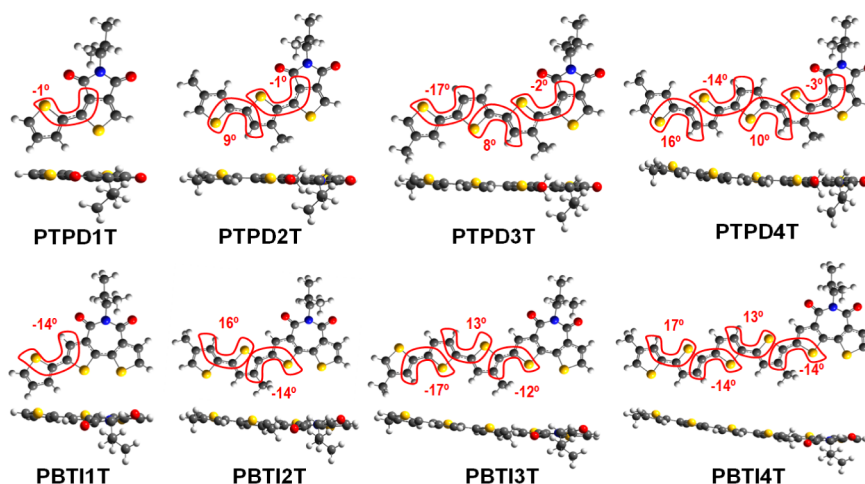
Figure 2. DFT//B3LYP/6-31G** computed **PTPDnT** (top) and **PBTInT** (bottom) repeating unit views perpendicular to the molecular planes with estimated dihedral angles between donor and acceptor moieties, as well as between nearby thiophene units in oligothiophene fragments. Repeating unit views in the molecular planes are also shown.
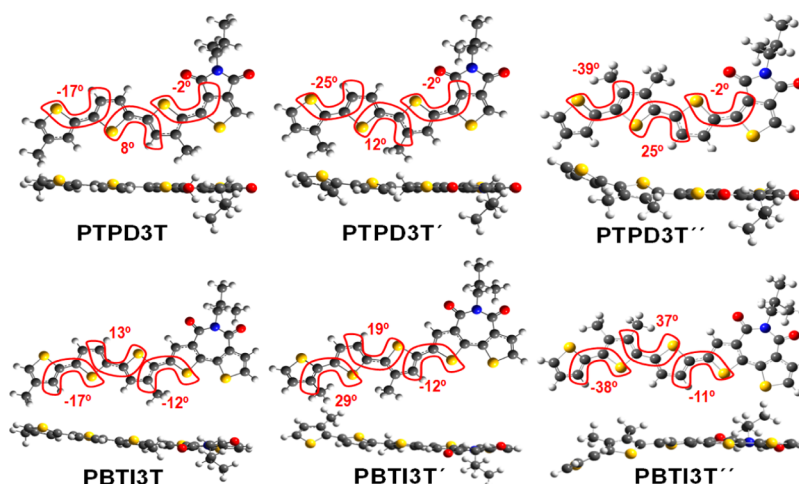
Figure 3. DFT//B3LYP/6-31G** optimized geometries for terthiophene-based **PTPD3T**, **PTPD3T′**, **PTPD3T″** (top), **PBTI3T**, **PBTI3T′**, and **PBTI3T″** (bottom). Repeating unit views in the molecular planes and perpendicular to the molecular planes are shown with estimated dihedral angles between donor and acceptor moieties, as well as between nearby thiophene units in oligothiophene fragments.

thiophene rings of **PTPD3T′**. This skeletal distortion is pronounced in **PTPD3T″**, where the two alkyl chains are installed at the β-positions of central thiophene. The high degree of skeletal distortion in **PTPD3T′** and **PTPD3T″** translates to reduced π-conjugation, as demonstrated by vibrational spectroscopy discussed below. A similar trend in skeletal distortion is also found for the **BTI** polymer analogues (Figure 3).

For a better estimation of polymer FMO levels, DFT calculations were also carried out on models having four repeating units. Table 2 summarizes the computed FMO energies as well as the reorganization energies for all polymers. These energies were estimated from calculations on monomeric models. Note that, for both **TPD** and **BTI** series, progressive addition of electron-rich thiophene gradually destabilizes both the HOMO and LUMO for all polymers. Furthermore, the thiophene addition also reduces the reorganization energies, λ_h, for hole transfer, favorable for increased hole mobilities[32,63] (Table 2). Please note that even if low values of reorganization energies are desirable for efficient charge transport, this parameter by itself cannot provide an accurate estimation of mobility values. In addition to reorganization energies, several other effects play roles in

determining mobility, such as molecular orientation and domain connectivity. Interestingly, **PTPD1T** and **PBTI1T** also exhibit small electron reorganization energies, λ_e, indicating their potential for electron transport.[31,64] In the case of **PTPD3T′**, **PTPD3T″**, **PBTI3T′**, and **PBTI3T″**, the reorganization energies gradually increase with decreased skeletal planarity.

Raman Spectroscopy. FT-Raman spectra of the present 12 polymers were investigated to probe the degree of π-conjugation within the series. In principle, more conjugated systems should exhibit enhanced charge transport capabilities due to enhanced skeletal planarity and more stabilized charge carriers. Although the total profile of the Raman spectra could be analyzed, the principal focus here is on the linear oligothiophene so-called "line B", according to the Effetive Coordinate (ECC) theory.[65] This band is assigned to the symmetric vibration of the thiophenic double and single bonds (ν_{sym} (C=C/C−C)) and has been widely used to assay the degree of π-conjugation in these systems.[66−70] Figure 4 compares the experimental and DFT//B3LYP/6-31G** computed Raman spectra for the **TPD** series. Note that while the computed spectra are for monomers, there is nevertheless good agreement between experimental and

Table 2. DFT Computed Energy Levels (Using Four Linked Comonomeric Units), Intermolecular Reorganization Energies (Using a Comonomeric Model) For Polymers PTPDnT and PBTInT; Experimental Energy Levels Derived from UPS and Optical Measurements Are Presented for Comparison

|	DFT calculation				Experimental	
Polymer	HOMO (eV)	LUMO (eV)	λ_h (eV)	λ_e (eV)	HOMO[a] (eV)	LUMO[b] (eV)
PTPD1T	−5.34	−2.91	0.38	0.36	−5.67	−3.94
PTPD2T	−4.91	−2.65	0.31	−	−5.47	−3.65
PTPD3T	−4.82	−2.64	0.30	−	−5.23	−3.41
PTPD3T′	−4.84	−2.69	0.35	−	−5.30	−3.48
PTPD3T″	−4.97	−2.60	0.43		−5.55	−3.73
PTPD4T	−4.79	−2.63	0.29	−	−5.23	−3.40
PBTI1T	−5.30	−3.05	0.35	0.47	−5.72	−3.85
PBTI2T	−5.00	−2.81	0.31	−	−5.57	−3.76
PBTI3T	−4.92	−2.79	0.29	−	−5.38	−3.56
PBTI3T′	−4.96	−2.80	0.37		−5.37	−3.55
PBTI3T″	−5.07	−2.76	0.44		−5.45	−3.63
PBTI4T	−4.88	−2.75	0.28	−	−5.25	−3.41

[a]HOMO values are determined from SECO and HOMO regions from UPS spectra shown in Figure 5a. [b]LUMO values are determined from $E_{LUMO} = HOMO + E_g^{opt}$.

theoretical data. The experimental **PTPD1T** FT-Raman spectrum exhibits a simple profile, with only two intense bands at 1517 and 1429 cm⁻¹. According to the DFT calculations, the high energy band not only corresponds to a vibration primarily localized on the **TPD** unit but also involves the thiophene ring in an asymmetric C−C vibration (ν_{asym} (C=C/C−C)) mode. In contrast, the 1429 cm⁻¹ band is assigned to the linear oligothiophene "line B", involving ν_{sym} (C=C/C−C), which provides a π-conjugation index. The insertion of a single thiophene in **PTPD2T** slightly complicates the Raman spectrum

with the appearance of three intense bands in the 1700−800 cm⁻¹ region (1503, 1435−1426, and 1394 cm⁻¹), with one peak consisting of two overlapping bands. The band at 1503 cm⁻¹ corresponds to that at 1517 cm⁻¹ in **PTPD1T**, while the 1426 shoulder corresponds to the 1429 cm⁻¹ band (line B) in **PTPD1T** and is localized primarily on the thiophene adjacent to the **TPD** unit. Importantly, both vibrations shift to lower energies on thiophene catenation, indicating a sizable π-extension.

The appearance of four peaks is evident in **PTPD3T** and **PTPD4T**, since the two vibrations that coalesce in **PTPD2T** are now completely resolved. Note that the mode centered in the **TPD** unit remains essentially unchanged on **nT** elongation—a 2 cm⁻¹ downshift occurs in **PTPD4T**, while the 1426 and 1394 cm⁻¹ thiophene vibrations in **PTPD2T** slightly downshift to 1421 and 1389 cm⁻¹ in **PTPD4T**. In contrast, the 1435 cm⁻¹ vibration in the **2T** derivatives upshifts to 1458 cm⁻¹ and becomes the most intense spectral feature. Note that, for **PTPD3T** and **PTPD4T**, the peak positions are almost identical, and the spectra profiles only differ in relative intensities. This similarity argues that the limit of π-conjugation between donor and acceptor subunits is reached at the **3T** polymer. Therefore, further oligothiophene catenation does not modify the donor−acceptor interaction strength. This result, as will be seen later, is in complete agreement with device performance, indicating that charge transport properties are gradually enhanced on increasing thiophene number up to **3**; however it decreases when an additional thiophene is added. Thus, in terms of π-conjugation, **PTPD3T** and **PTPD4T** are basically identical; however, increasing oligothiophene length lowers the skeletal planarity (see calculations mentioned above and Figure 2), and thus molecular close-packing and charge transport may be reduced.

The effects of the alkylation pattern on π-conjugation were next probed by Raman in **PTPD3T**, **PTPD3T′**, and **PTPD3T″**. As noted in the DFT calculations, a change in the alkylation pattern from "outward" in **PTPD3T** to "inward" in **PTPD3T′**
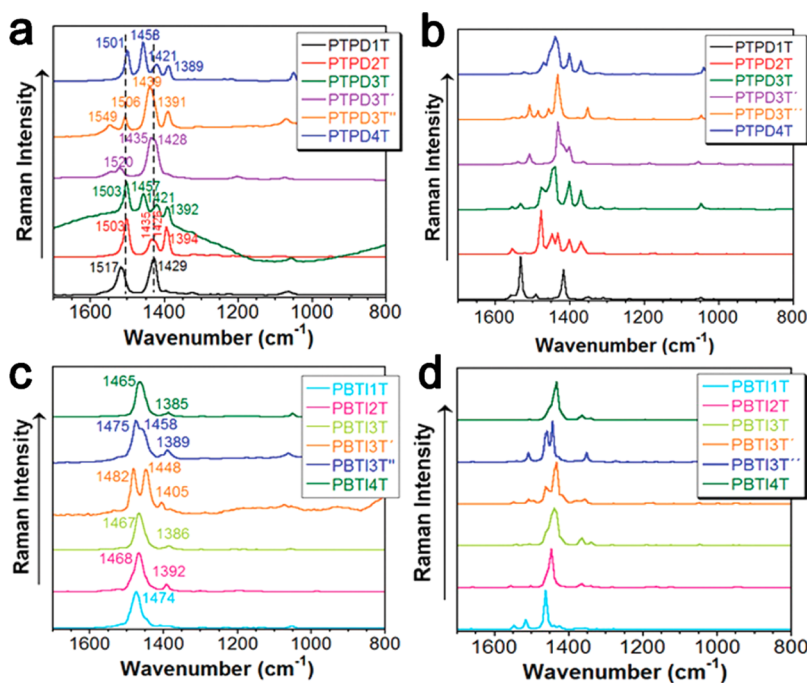
Figure 4. Experimental FT-Raman spectra recorded for the (a) **PTPDnT** and (c) **PBTInT** polymers. DFT//B3LYP/6-31G** simulated Raman spectra on the comonomeric units of the (b) **PTPDnT** and (d) **PBTInT** polymers.
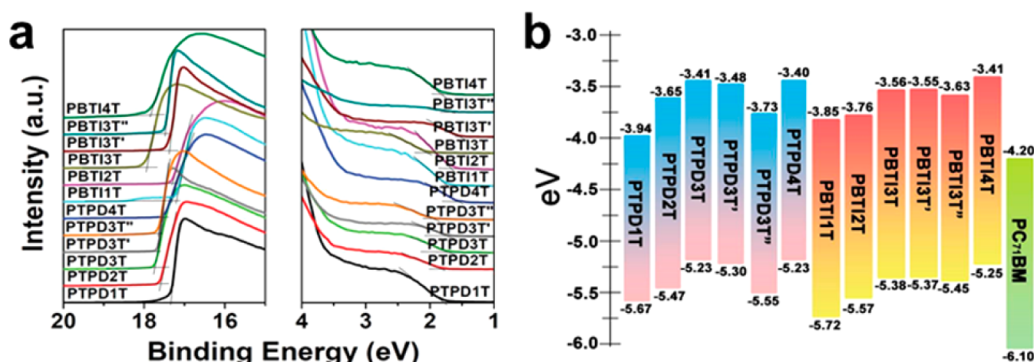
Figure 5. (a) UPS of **PTPDnT** and **PBTInT** polymer thin films spun cast from chloroform (5 mg/mL); (b) Experimentally determined energy levels derived from UPS and optical absorption measurements.

translates into backbone distortion between the thiophene rings. This skeletal distortion is further evidenced when both central thiophene β-positions are alkylated. In fact, the computed interthiophene dihedral angles increase from 8° and −17° in **PTPD3T** to 12° and −25° in **PTPD3T′** and to 25° and −39° in **PTPD3T″**. Moving from **PTPD3T** to **PTPD3T′**, the acceptor unit vibrational mode is upshifted by 17 cm^{-1}, indicating reduced donor−acceptor π-conjugation for the "inward" derivative, in accord with the reduced skeletal planarity predicted for **PTPD3T′**.[71] Furthermore, the oligothiophene chain vibrations coalesce into a single intense band near 1428−1435 cm^{-1}, further confirmation of impeded π-conjugation versus **PTPD3T**, which is in good agreement with their optical absorption. Note that this vibrational mode is further upshifted to 1439 cm^{-1} for **PTPD3T″**, in good agreement with a more distorted skeleton and decreased π-conjugation.

The **BTI** series also evidences good agreement between experiment and theory (Figure 4c and 4d), with a simple FT-Raman profile. The **PBTI1T** spectrum is dominated by an intense 1474 cm^{-1} band arising from a symmetric thiophene ring C=C/C−C mode, assignable to Line B. This thiophene/oligothiophene feature is the most intense in the series and significantly downshifts from 1474 to 1468 cm^{-1} from **PBTI1T** to **PBTI2T**. However, on chain elongation to **PBTI4T**, the frequency remains almost unaltered, suggesting similar π-conjugation in **PBTI2T**, **PBTI3T**, and **PBTI4T**. On comparing **PBTI3T**, **PBTI3T′**, and **PBTI3T″**, the effects of the differing alkylation pattern are evident. Note that DFT predicts that "inward" substitution causes skeletal distortion of the interthiophene dihedral angle of 19° and 29°, while dihedral angles of only 13° and −17° are predicted for the "outward" substitution. Greater skeletal distortion is computed for **PBTI3T″**, where central thiophene ring double alkylation gives dihedral angles of 37° and −38°. These geometrical changes are evident in the Raman spectra, where line B splits in **PBTI3T′** and **PBTI3T″** into well-separated bands at 1482 and 1448 cm^{-1}, and 1475 and 1458 cm^{-1}, respectively. The highest energy mode corresponds to a symmetric C=C/C−C vibration of the **BTI** thiophene rings and the first thiophene appended to the electron-withdrawing group. The appearance of this vibration at higher energies than in **PBTI3T** indicates the disruption of the π-conjugation due to oligothiophene backbone distortions by the differing alkylation patterns, in agreement with the lower device performance (*vide infra*).

Polymer Energy Levels. UV photoemission spectroscopy (UPS) was employed to obtain information on polymer HOMO energies (He I excitation source, hν = 21.22 eV). Figure 5a shows the secondary electron cutoff (SECO) and HOMO regions for all polymers, and Figure 5b shows the corresponding band energy alignment. As expected, the thiophene catenation gradually increases HOMOs for both **PTPDnT** and **PBTInT** series (Table 2). For the **PTPDnT** series, the HOMOs vary from −5.67 eV to −5.23 eV, whereas, for the **PBTInT** series, the HOMOs change from −5.72 to −5.25 eV. Both HOMO and LUMO (calculated from $E_{LUMO} = E_{HOMO} + E_g^{opt}$) are in excellent agreement with the values obtained from DFT calculations. When comparing **PTPDnT** and **PBTInT** polymers having the same **nT**s as the donor co-units, note that the **PBTInT** polymer series typically has lower-lying HOMOs, reflecting their greater degree of backbone torsion[35,39,72] due to the S···O interaction absence. Analysis of alkylation regiochemistry in the **3T** polymers shows that the HOMOs of the "inward" alkylated derivatives **PTPD3T′** and **PBTI3T′** are comparable to those of the "outward" derivatives **PTPD3T** and **PBTI3T**, respectively. However, the polymers with the alkylation on the β-positions of the central thiophene, **PTPD3T″** and **PBTI3T″**, both show significantly lowered HOMOs. This result is in good agreement with the DFT calculated HOMO energies, especially trends due to backbone nonplanarity (Table 2). Polymers having greater backbone torsion have lower-lying HOMOs due to the reduced electron delocalization.[39,72]

Charge Transport Characteristics. Polymer charge transport characteristics were evaluated in both thin-film transistors (TFTs) and space-charge limited current (SCLC) diodes, and the relevant mobilities are summarized in Table 3. **1T**-based polymers **PTPD1T** and **PBTI1T** exhibit low $\mu_{h,FET}$ of 2.8×10^{-3} and 7.1×10^{-5} cm^2/(V s), respectively. Thiophene addition leads to enhanced hole transport, but negligible electron transport, for **PTPD2T** and **PBTI2T** with $\mu_{h,FET}$ of 6.2×10^{-3} and 1.1×10^{-3} cm^2/(V s), respectively. For the **3T** polymers, **PTPD3T** and **PBTI3T** exhibit substantial $\mu_{h,FET}$ of 0.10 and 9.2×10^{-2} cm^2/(V s), respectively, the highest values in their respective series; further thiophene addition results in **4T** polymers with slightly decreased mobility. Not unexpectedly, the isomeric **3T** polymer derivatives exhibit significantly lower mobilities [$\mu_{h,FET}$ (cm^2/(V s)) = 4.7×10^{-6} (**PTPD3T′**), 1.9×10^{-2} (**PTPD3T″**), 5.6×10^{-3} (**PBTI3T′**), and 5.3×10^{-3} (**PBTI3T″**)]. The lowest **PTPD3T′** mobility is in good agreement with its most blue-shifted absorption. These OTFT results are in good accord with the backbone planarity, conjugation level, degree of crystallinity, and long-range ordering described above. In comparison to **BTI** polymers, **TPD** polymers typically show higher mobility, which is attributed to the greater backbone planarity enabled by intramolecular S···O interactions in **TPD** polymers.

Table 3. Summary of SCLC, TFT, and PSC Performance Metrics for PTPDnT and PBTInT Polymers

Polymer	Charge transport characteristics			PSC characteristics			
	μ_{FET} (cm^2/(V s))[a]	μ_{SCLC} (neat) (cm^2/(V s))	μ_{SCLC} (blend) (cm^2/(V s))	V_{oc} (V)	J_{sc} (mA/cm^2)	FF (%)	PCE (%)[b]
PTPD1T	2.8×10^{-3}	3.2×10^{-5}	1.7×10^{-6}	0.59	1.75	33.4	0.35 (0.31)
PTPD2T	6.2×10^{-3}	2.0×10^{-4}	1.7×10^{-4}	0.90	8.92	70.7	5.66 (5.35)
PTPD3T	0.10	3.1×10^{-3}	2.7×10^{-3}	0.79	12.3	79.5	7.73 (7.54)
PTPD3T′	4.7×10^{-6}	1.0×10^{-6}	9.5×10^{-7}	0.78	0.980	45.0	0.34 (0.29)
PTPD3T″	1.9×10^{-2}	2.4×10^{-3}	1.5×10^{-3}	0.81	2.53	50.6	1.04 (0.98)
PTPD4T	4.4×10^{-2}	9.8×10^{-4}	7.4×10^{-4}	0.65	7.47	66.9	3.26 (3.18)
PBTI1T	7.1×10^{-5}	2.1×10^{-5}	9.3×10^{-7}	0.75	0.71	30.9	0.16 (0.15)
PBTI2T	1.1×10^{-3}	1.9×10^{-4}	1.6×10^{-4}	0.95	8.15	69.4	5.37 (5.11)
PBTI3T	9.2×10^{-2}	2.1×10^{-3}	1.5×10^{-3}	0.86	11.8	75.9	7.70 (7.38)
PBTI3T′	5.6×10^{-3}	7.5×10^{-4}	2.8×10^{-4}	0.79	1.81	49.4	0.71 (0.62)
PBTI3T″	5.3×10^{-3}	6.6×10^{-4}	3.2×10^{-4}	0.78	2.90	45.7	1.03 (1.00)
PBTI4T	7.1×10^{-2}	8.3×10^{-4}	6.7×10^{-4}	0.75	9.30	68.4	4.74 (4.67)

[a]Average of at least five devices, the TFT using neat polymer film as the active layer. [b]All PSCs use inverted device architecture: ITO/ZnO/active layer/MoO$_3$/Ag. Active layers spun-cast from a polymer:PC$_{71}$BM = 1:2 solutions, except for **PBTI1T** and **PTPD1T** which were cast from a polymer:PC$_{71}$BM = 1:1 from CF/DIO (98%:2%, v/v) solution. Data represent best performing device, and average values of at least eight devices are shown in parentheses.
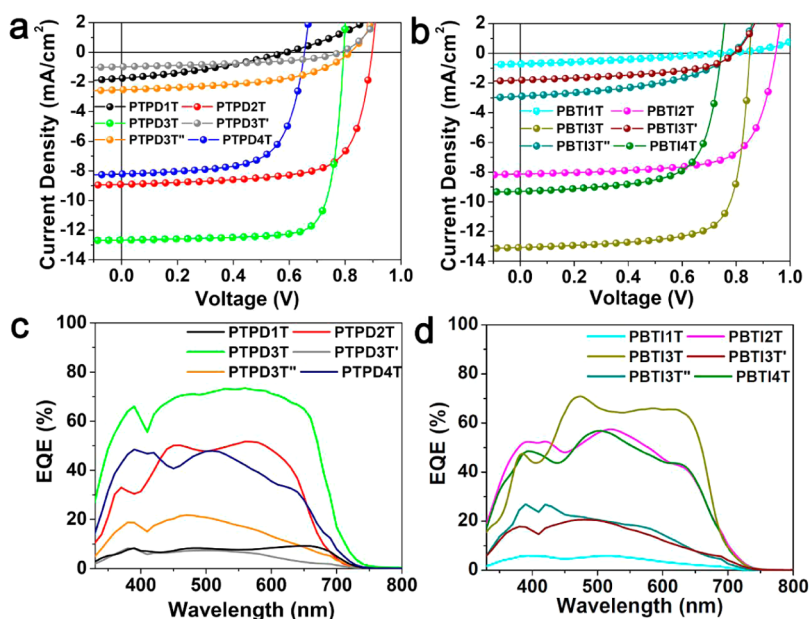
Figure 6. Inverted PSC performance. (a, b) Illuminated $J-V$ characteristics of optimized **PTPDnT**:PC$_{71}$BM and **PBTInT**:PC$_{71}$BM devices fabricated with chloroform (CF):diiodooctane (DIO) (98:2 v/v) as the solvent; (c, d) external quantum efficiency of corresponding PSCs.

The TFT mobility data offer insights on polymer backbone planarity and film crystallinity. In addition to TFT measurements, SCLC mobility in diode architecture was measured to evaluate charge transport perpendicular to the substrate, which is more relevant for PSC operation.[73,74] Hole-only diodes were fabricated using the structure of ITO/PEDOT:PSS/polymer (or polymer:PCBM)/MoO$_3$/Au, and the SCLC mobilities are summarized in Table 3. The overall SCLC mobility trends of neat polymer films are consistent with the OTFT mobility, showing the highest $\mu_{h,SCLC}$ of 3.1×10^{-3} and 2.1×10^{-3} cm^2/(V s) for **PTPD3T** and **PBTI3T** in their respective series, respectively, and **PTPD3T′** again shows the lowest $\mu_{h,SCLC}$ of 1.0×10^{-6} cm^2/(V s). The polymer:PCBM blend films show slightly lower SCLC mobilities than those of neat polymer films with comparable trends (Table 3). For example, $\mu_{h,SCLC}$ of 2.7×10^{-3} and 1.5×10^{-3} cm^2/(V s) are obtained for **PTPD3T** and **PBTI3T** blends, respectively, which are the highest in their respective series.

Polymer Solar Cell Response. All polymers were first evaluated in inverted BHJ PSCs having an architecture of ITO/ZnO/active layer/MoO$_3$/Ag. The cells were fabricated by spin-casting polymer:PC$_{71}$BM CHCl$_3$ solutions with a polymer concentration of ∼5 mg/mL. The active layers were unannealed prior to thermal evaporation of the MoO$_3$/Ag (7.5 nm/120 nm) anode. PSC optimization was mainly carried out using the processing additive, 1,8-diiodooctane (DIO), which often improves blend film morphology.[51,75−77] From our previous studies of **PTPD3T** and **PBTI3T** PSCs,[35] the PC$_{71}$BM domain size can be significantly reduced using a small amount of DIO. For the complete **TPD** and **BTI** series, DIO addition consistently improves blend film morphology. AFM topographical images of the blend films processed without DIO (Figure S5) and those processed with 2% DIO (Figure S6) reveal that the latter evidence reduced roughness and more homogeneous polymer donor/PCBM acceptor domain distributions (*vide infra*).
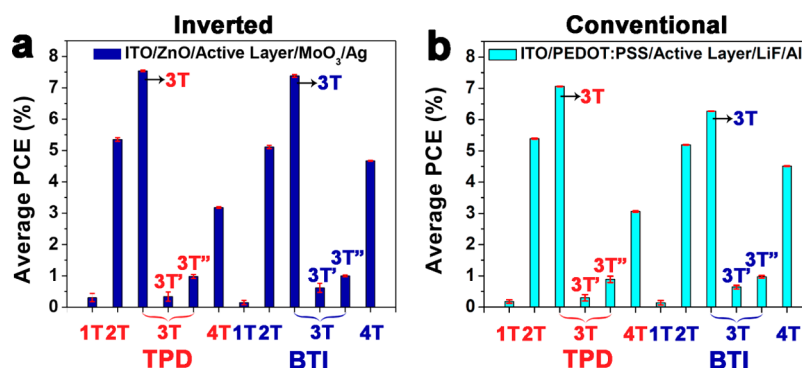
Figure 7. Comparison of (a) inverted and (b) conventional PSC performance for optimized **PTPDnT**:PC$_{71}$BM and **PBTInT**:PC$_{71}$BM blends.

PSCs were optimized by screening different polymer:PCBM ratios from 1:1 to 1:3, and the best performance was achieved with a ratio of 1:2 for all polymers except for **PTPD1T** and **PBTI1T** where the optimum ratio was found to be 1:1. All devices were fabricated using chloroform (CF):DIO (98%:2%, v/v) as the solvent. Figure 6 shows the current−voltage (J−V) characteristics and external quantum efficiency of optimized PSCs, and relevant photovoltaic data are collected in Table 3.

Not unexpectedly, the **1T**-based polymers **PTPD1T** and **PBTI1T** exhibit low PCEs of <0.5%, owing to their relatively low hole mobilities. Furthermore, from energetic considerations, the driving force for exciton separation may be insufficient, leading to poor charge carrier generation.[73,78,79] Despite the lowest-lying HOMOs of **1T**-based polmers, **PBTI1T** and **PTPD1T** PSCs show the smallest V_{oc}s in their respective series, which is attributed to the significant charge recombination due to their low mobility and ambipolar transport characteristics.[80,81] With added thiophene rings, the LUMO(donor)-LUMO(acceptor) offset is enlarged and these polymers exhibit greatly increased hole mobilities. Both **PTPD2T** and **PBTI2T** show dramatically enhanced PCEs 5.66% and 5.37%, respectively. Note that the **PTPD2T** PCE is smaller than that (7.3%) of TPD-bithiophene analogue reported by Wei et al.,[56] in which a smaller 2-ethylhexyl is attached to the **TPD** block. Reflecting the **PTPD2T** and **PBTI2T** deep-lying HOMOs of −5.47 and −5.57 eV, the corresponding cells show very high V_{oc}s of 0.90 and 0.95 V, respectively. The large V_{oc}s illustrate the advantages of the strong electron-withdrawing **TPD** and **BTI** units for high V_{oc} copolymers.[6,20,23,82] Furthermore, these two polymers also exhibit high FFs of 70.7% and 69.4%, respectively. The slightly higher **PTPD2T** FF versus that of **PBTI2T** is consistent with the higher degree of **PTPD2T** crystallinity.

On proceeding from **2T** to **3T** systems, **PTPD3T** shows an excellent PCE = 7.73%. Despite a slightly reduced V_{oc} = 0.79 V due to the higher-lying HOMO of −5.23 eV versus that (−5.47 eV) of **PTPD2T**, the increased PCE is attributed to the significantly enhanced J_{sc} (12.3 cm^2/(V s)) and FF (79.5%). Similarly, **PBTI3T** exhibits the highest PCE in **BTI** series, up to 7.70% owing to the high J_{sc} (11.8 cm^2/(V s)) and FF (75.9%). Note that this PCE is lower than the previous result for **PBTI3T** having a shorter *n*-decyl chain installed at the **3T** unit[35] and demonstrates the impact of the solubilizing substituent on PCE.[6,11] In the community, it is well-known that the polymer molecular weight (M_n) is an important parameter that can affect device performance. In general, higher M_n polymers give better performance. In order to eliminate the M_n effect, **PTPD3T** with a M_n of 30 kDa was also synthesized, which shows a greater J_{sc} (12.0 cm^2/(V s)) and FF (78.3%) than **PBTI3T** with

comparable M_n (27.4 kDa). Therefore, the extremely high FF of **PTPD3T** PSCs is not only due to its high M_n but also the unique film morphology and microstructure, which also play significant roles. Further thiophene addition from **3T** to **4T** lowers performance for both **PTPD4T** and **PBTI4T** with respect to the **3T** counterparts, affording PCEs of 3.26% and 4.74% for **PTPD4T** and **PBTI4T**, respectively. In compasison to the performance parameters of **4T**-based polymers, **3T**-based polymers show higher V_{oc}'s due to the weaker electron-donating ability of **3T** (versus **4T**), and greater J_{sc}'s and FFs are attributed to the higher mobilities of **3T** polymers. Therefore, **3T** is the optimal donor unit among all **nTs** in the **PBTInT** and **PTPDnT** polymer series for PSCs. It is also instructive to compare the PSC performance variations induced by alkylation regiochemistry for the **3T** polymer isomers. Consistent with their inferior absorption and lower mobilities, the "inward" **PTPD3T′** and **PBTI3T′** isomers deliver low PCEs of 0.34% and 0.71%, respectively, whereas the isomeric **PTPD3T″** and **PBTI3T″** provide only slightly increased PCEs of 1.04% and 1.03%, respectively. Therefore, among all terthiophene units, **3T** with an "outward" alkylation pattern benefits performance due to the resulting polymers with increased conjugation and better materials packing.

In addition to the above inverted cells, conventional PSCs were fabricated in the architecture, ITO/PEDOT:PSS/active layer/LiF/Al, and the resulting cells exhibit inferior PSC performance characteristics (Figure 7b and Table S3) versus the inverted ones. In a previous work[35] we observed vertical BHJ phase segregation and PC$_{71}$BM enrichment near the n-type ZnO IFL surface, clearly an advantage of the inverted architecture and attributable to the different polymer and PC$_{71}$BM surface energies. To further understand differences in vertical morphology evolution for the same active layer films, **PTPD3T**:PC$_{71}$BM and **PBTI3T**:PC$_{71}$BM were cast on ZnO- and PEDOT:PSS-modified substrates, and XPS depth profile analysis was performed, proceeding from the blend/air interface, through the blend films, and finally to the ZnO or PEDOT:PSS (Figure S10). Compared to the previously reported XPS depth profiles for inverted cells,[35] the conventional cells have a thin polymer overlayer indicated by a strong S signal at the air/blend interface, then an essentially constant S/C ratio throughout the active layers (Figure S11). Indeed, the contact angle measurements as in the previous report[35] reveal that both polymers and PC$_{71}$BM have excellent wettability and similar wetting parameters, ΔW, varying from −1.29 to −1.45 mN/m on PEDOT:PSS surfaces, implying the absence of characteristics favorable to the vertical phase gradient in the conventional cell architectures.

Morphological Characterization of Polymer Films. High-resolution TEM (HR-TEM) imaging was carried out to elucidate the microstructure of as-cast neat polymer films. All specimens (∼30 nm) were prepared by spin-coating polymer solutions without post-treatment, and TEM imaging was performed with slight defocus (∼5 μm) where the phase contrast is optimized for resolutions down to <1 nm. Figure S2 shows representative TEM images of the **PTPDnT** and **PBTInT** neat films. It can be readily seen that, except for **PBTI1T**, all polymers exhibit significant crystalline features. In particular, **PTPD3T** and **PTPD4T** both show observable lattice planes >10 nm (representative red circled areas). Compared to the **PBTInT** series, the **PTPDnT** series shows remarkable long-range order, corresponding to its more regular local interchain stacking, consistent with its greater coplanarity and more straight backbone.[26] Based on the molecular geometry described above, the more planar and straight **PTPDnT** backbone should favor stronger interpolymer interactions and higher degrees of crystallinity, which would, all other things being equal, lead to enhanced charge transport.

Active layer morphology was also investigated for all polymer blends by TEM (Figure 8). Similar to the HR-TEM images
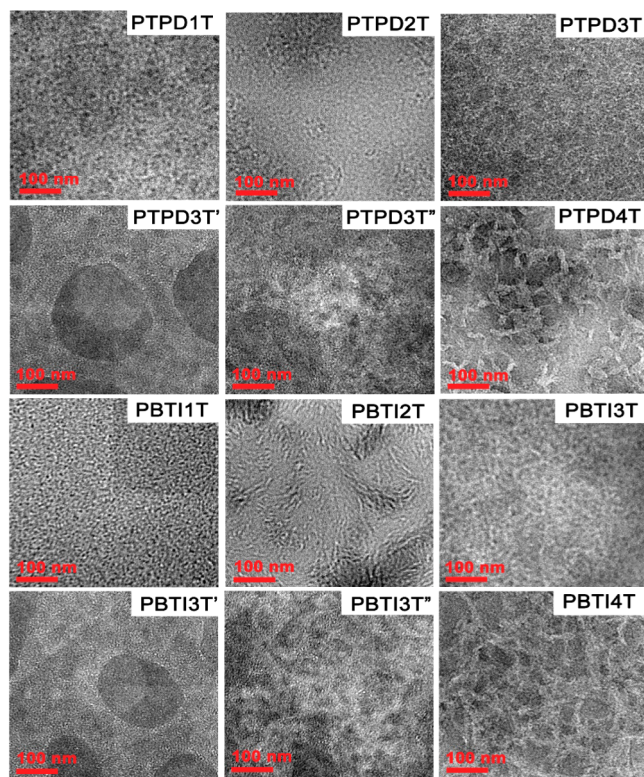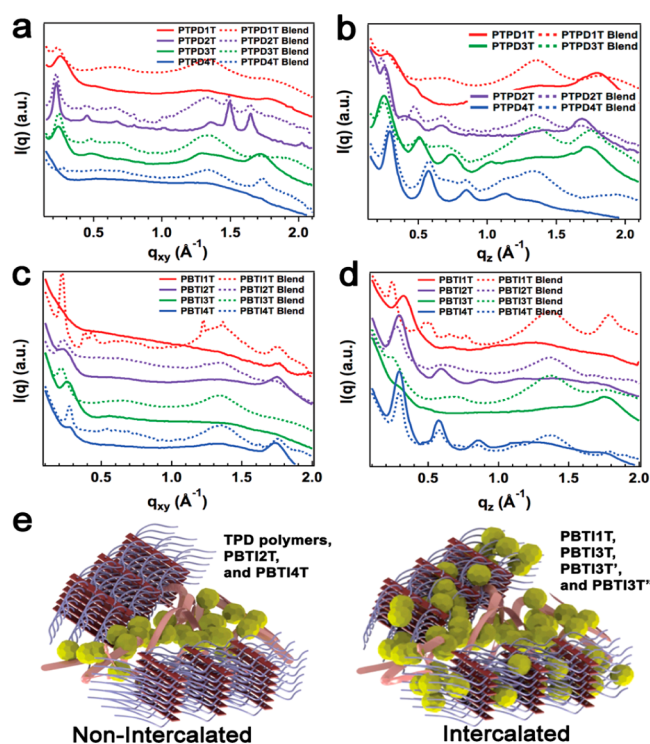

Figure 8. TEM images of **PTPDnT** and **PBTInT** blend films prepared with DIO as the processing addtive, under the same conditions as the actual PSC fabrication.

(Figure S2) of the neat films dicussed above, the blend films of both **TPD** and **BTI** series with **2T**, **3T**, and **4T** units exhibit relatively high crystallinity, implying that the semicrystalline features of the neat polymers are conserved in the blend films. Interestingly, different degrees of polymer:fullerene phase separation are found in the blend films with polymers employing **2T**, **3T**, and **4T** units. Specifically, both **PTPD2T** and **PBTI2T** blends exhibit relatively large phase separated regions having pure fullerene and semicrystalline polymer domains. This result

is not unexpected since the close-packed **2T** unit side chains may exclude the fullerene from the polymer backbone regions.[83] Inserting an additional thiophene in the **PTPD3T** and **PBTI3T** repeat units leads to significantly finer blend film morphologies with relatively small polymer−fullerene domains. Especially for **PTPD3T**, the BHJ blends consist of continuous nanofibrillar polymer networks, which is ideal for charge transport, yielding high J_{sc} and FF metrics for the corresponding PSCs. Further oligothiophene extension to **4T** results in large semicrystalline polymer domains (Figure 8). Despite the percolated morphology of these **4T**-based blends, the relatively large domains result in small donor−acceptor interfaces for exciton separation, reflected in the relatively lower PL quenching efficiencies (Figures S12−S14). By extending this analysis to the isomeric **3T′** and **3T″** polymer blends, dramatically different morphologies are observed versus those observed for the **3Ts**. Specifically, both **3T′** polymers exhibit relatively large degrees of phase separation, whereas the two **3T″** polymers have well mixed microstructures, but less ordered morphologies compared to the **3T** polymers.

To gain further insight into film morphology, grazing incident wide-angle X-ray scattering (GIWAXS) analyses were performed on neat and blend films (Figures 9 and 10). The measured $\pi-\pi$ and lamellar stacking distances are summarized in Table S4. On the basis of the lamellar spacings of the neat films, the

Figure 9. GIWAXS characterization of neat and blend films for **PTPDnT** and **PBTInT** varying the number of thiophenes. (a) In-plane and (b) out-of-plane line-cuts comparing neat and blend films based on **PTPDnT**; (c) in-plane and (d) out-of-plane line-cuts comparing neat and blend films based on **PBTInT**; (e) schematic representation of nonintercalated and intercalated cases, representing polymer and fullerene mixing either in amorphous polymer regions or in both amorphous and crystalline regions. Note: the two sharp features at $q_{xy} \approx 1.5$ for in plane **PTPD2T** are from the substrate. The blend films prepared with DIO as the processing additive, under the same conditions as the actual PSC fabrication.
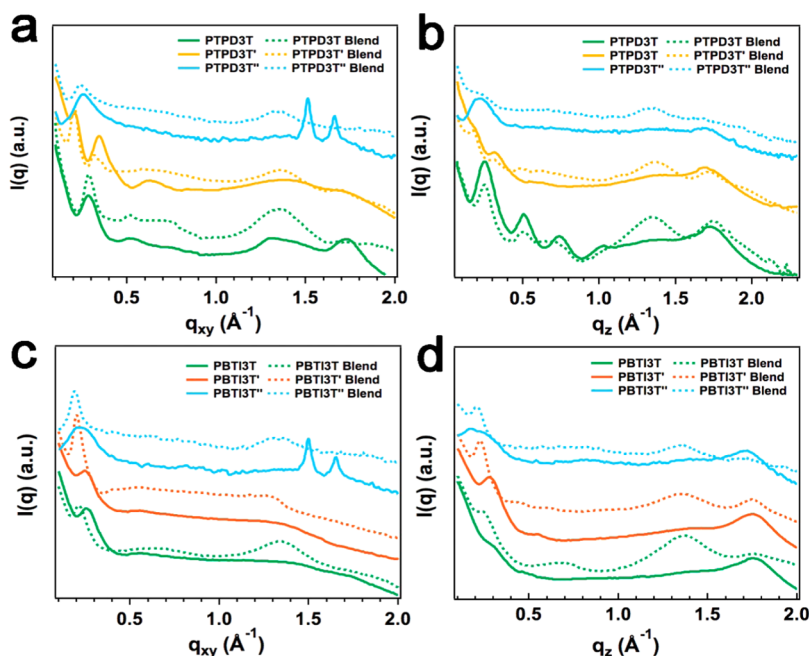
Figure 10. GIWAXS characterization of neat and blend films for **3T** polymer derivatives, including **PTPD3T**, **PTPD3T′**, **PTPD3T″**, **PBTI3T**, **PBTI3T′**, and **PBTI3T″**; (a) in-plane and (b) out-of-plane line-cuts comparing neat and blend films based on **PTPD3T**, **PTPD3T′**, and **PTPD3T″**; (c) in-plane and (d) out-of-plane line-cuts comparing neat and blend films based on **PBTI3T**, **PBTI3T′**, and **PBTI3T″**. The blend films prepared with DIO as the processing additive, under the same conditions as the actual PSC fabrication.

polymers tend to have a higher degree of interdigitation due to the enlarged spacings between the alkyl chains as the thiophene number increases from **2T** to **4T**. For the blend **TPD** polymer films, **PTPD1T**, **PTPD2T**, and **PTPD3T** show a predominantly π-face-on orientation of the polymer chains, characterized by strong out-of-plane π−π stacking peaks, whereas the **PTPD4T** blend film takes on a preferential edge-on orientation with respect to the substrate surface. Furthermore, the thiophene addition gradually enhances polymer film crystallinity, with both **PTPD3T** and **PTPD4T** films showing (100), (200), and (300) Bragg reflections. Furthermore, proceeding from the **2T** to the **4T** based polymers incrementally contracts the π−π stacking distances, again suggesting strong polymer−polymer interactions for **PTPD3T** and **PTPD4T**. The **BTI** polymer films are, in agreement with the TEM images (Figure S2), less crystalline than the corresponding **TPD** polymers, correlating with their reduced backbone planarity and more curved backbone. The **PBTI1T**, **PBTI2T**, and **PBTI4T** blend films show predominantly in-plane π-stacking peaks, indicating an edge-on orientation, whereas **PBTI3T** shows a distinctly different face-on orientation. The diffraction patterns of the blend films show that **PTPD2T** adopts a π-face-on preferred orientation, while **PBTI2T** assumes a π-edge-on preferred orientation. Although it is known that π-face-on is beneficial to charge transport and extraction in solar cells, the **PBTI2T** PSC shows comparable *FF* and J_{sc} to those of **PTPD2T** PSC, which is likely attributed to its more compact π-stacking (3.60 Å) and lamellar (23.1 Å) distance of the **PBTI2T** blend film versus those (π-stacking = 3.74 Å; lamellar = 28 Å) of the **PTPD2T** blend film. Moreover, **PBTI2T** could have greater intramolecular and intermolecular π-orbital overlap due to the fused **BTI** unit, which facilitates charge delocalization and hence increases mobility and *FF* in **PBTI2T** cells. As a result, comparable J_{sc}'s and *FF*s were obtained from **PTPD2T** and **PBTI2T** PSCs. Comparing the correlation lengths calculated using Scherrer analysis[84] for blend films reveals that **PTPD4T** and **PBTI4T**

possess the largest domain sizes of their respective polymer series, in excellent agreement with the TEM measurement (Figure 8); thus not surprisingly, these two polymers show relatively low J_{sc}'s despite their high crystallinity.

Although both the **TPD** and **BTI** polymer series show similar PSC performance trends when varying the oligothiophene length, the morphological and charge transport characteristics show some difference between the two series. Comparing the two best performing polymers, **PTPD3T** and **PBTI3T**, if the differences in V_{oc}'s induced by their HOMO energies are ignored, **PTPD3T** shows clear superiority over **PBTI3T** in its high *FF* and J_{sc}. These two metrics account for a >9% difference in PCEs. According to McGehee's results,[83,85] comparing donor polymer *d*-spacings before and after blending with fullerene provides information on the extent of fullerene molecule intercalation between polymer side chains. Following this approach, the change in lamellar spacing was systematically investigated by 2D GIWAXS for the present films (Figures 9 and 10). Remarkably, all **TPD** polymers exhibit identical lamellar spacings in the neat and blend films, suggesting that the local crystalline phases are relatively intact (Figure 9e). However, noticeable 4.6−6.4 Å lamellar expansions are observed for all **BTI** polymers with the exception of **PBTI2T** and **PBTI4T**. Thus, the rigidity of the **TPD** based polymer backbone plays an important role in preventing bimolecular crystal formation in which fullerenes are extensively intercalated between the polymer side chains.[86] Therefore, for the **TPD** polymer blends, the fullerenes are predominantly present in an amorphous polymer phase and/or fullerene-rich domain. In contrast, for the **BTI** polymer blends, the reduced backbone coplanarity with a higher degree of curvature appears to be responsible for the greater degree of PC$_{71}$BM intercalation.[86] When comparing the crystallinity after blending with PC$_{71}$BM, the polymers which do not undergo significant fullerene intercalation (all **TPD** polymers, **PBTI2T**, and **PBTI4T**) generally maintain the high level of crystallinity
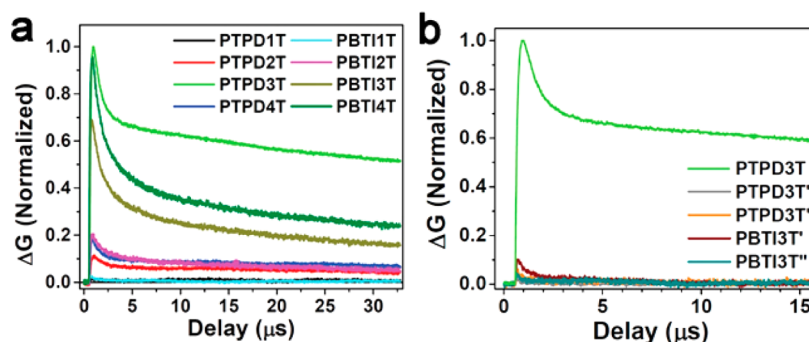
Figure 11. TRMC transients for (a) **PTPDnT** and **PBTInT** blends with $PC_{71}BM$, varying the thiophene catenation. (b) **3T** polymer derivatives, including **PTPD3T′**, **PTPD3T″**, **PBTI3T′**, and **PBTI3T″** blends with $PC_{71}BM$. The TRMC transient for **PTPD3T** is replotted from (a) for reference.

observed in the pristine films. Interestingly, relatively high *FF*s of 66.9% −79.5% are found for the **PTPDnT** ($n = 2−4$) blends, as well as for **PBTI2T** and **PBTI4T**, and the polymer with the highest *FF* approaching 80%, **PTPD3T**, displays substantial nonintercalated polymer crystalline regions. This finding argues that the formation of bimolecular crystal phases is far from the ideal polymer:fullerene blend film morphology.[87] Preventing substantial fullerene intercalation affords blend films with purer polymer and/or fullerene domains, which can lead to reduced bimolecular recombination and increased *FF*s.[88] For the most efficient polymer, **PTPD3T**, the presence of small polymer crystalline phases (correlation length = 6.6 and 11.8 Å, in neat and blend films, respectively), preserved after blending with $PC_{71}BM$, favors efficient charge transport with low recombination losses.

The in-plane (q_{xy}) and out-of-plane (q_z) line cuts for the 2D GIWAXS data for the isomeric **3T** based polymers are shown in Figure 10 (the 2D images are provided in Figure S7) and clearly reveal that the alkylation regiochemistry dramatically alters the polymer packing characteristics. When focusing on the (100) *d*-spacings, the alkyl substitution facing "inward" (**3T′**) and alkylation on the *β*-position of the central thiophene significantly expand, versus **PTPD3T** (26.3 Å) and **PBTI3T** (24.6 Å), the lamellar distances for **PTPD3T′**, **PTPD3T″**, **PBTI3T′** and **PBTI3T″** to 40.7, 28.8, 26.4, and 27.9 Å, respectively. Among the **3T** isomeric polymers, the "outward" polymers **PTDP3T** ad **PBTI3T** show the highest degree of interdigitation in their respective series, while **PTPD3T′** has a very large *d*-spacing of 40.7 Å, which is almost double that of **PTPD4T**, indicating almost no interdigitation in **PTPD3T′**. The result demonstrates that the steric hindrance is significantly reduced in **PTPD3T** due to the larger spacings between the side chains[33,64] and the opposite chain orientations. As the size of the acceptor unit expands, **PBTI3T′** has a much smaller *d*-spacing of 26.4 Å versus **PTPD3T′**. Additionally, when comparing *π*−*π* stacking distances, the **3T′** and **3T″** analogs show a 0.02−0.12 Å expansion versus the "outward" substituted **3T** polymers **PTPD3T** and **PBTI3T**. The result is in good agreement with their absorption evolution, charge arrier mobility, and solar cell performance.

Charge Carrier Dynamics. To characterize "intrinsic" charge transport in blend films without fabricating actual devices, Seki and co-workers recently argued that time-resolved microwave conductivity (TRMC) allows for the direct evaluation of BHJ PSC active layers without interference by macroscopic grain boundaries, impurities, and electrical contacts.[89,90] By carefully examining the temporal decay of the photoexcited carriers, it is possible to extract the carrier mobility, concentration, and lifetime in BHJ PSC active layers.[91−93] To study the charge transport characteristics of different active layers, we adopted a

similar TRMC probe to investigate the photoconductance, ΔG, and bimolecular recombination constant, k_{rec}, in the present materials rather than probing the carrier mobility and concentrations individually.[94] Unlike an electron paramagnetic resonance (EPR) experiment which measures the absorption of the microwave magnetic field component, TRMC measures the absorption of the electric field component which is proportional to conductivity.[95,96] In this work, the relative photoconductance values, ΔG, are compared for BHJ blend films in the **PTPDnT** and **PBTInT** series. Note here that the end-of-pulse (peak) photoconductivity signal, ΔG_{max}, is proportional to the product of the charge carrier yield, ϕ, and the sum of high-frequency electron/hole mobilities, $\Sigma\mu$ (eq 1).[97,98]

$$\Delta G_{max} = \beta q_e \times I_0 F_A \times \phi\Sigma\mu \quad (1)$$

In Figure 11a the TRMC BHJ transients show that **PTPD3T** has the highest ΔG value of all the polymers, indicating a higher carrier concentration and/or higher carrier mobility, both being significant metrics of high PSC performance. More importantly, the value of ΔG_{max} for **PTPD3T** is ∼5× higher than that of **PTPD4T** and ∼10× higher than that of **PTPD2T**. Furthermore, for the **BTI** series, **PBTI4T** shows a larger ΔG_{max} than the best-performing **PBTI3T** in this series, although it is lower than that of **PTPD3T**. We note that although the FET mobilities of these two polymers are similar (**PBTI3T**, 9.2×10^{-2} vs **PBTI4T**, 7.1×10^{-2} cm^2/(V s)), the fact that **PBTI4T** maintains nonintercalated polymer crystalline domains agrees well with this metric of higher local mobility.[99] For the **3T′** and **3T″** derivatives, interestingly, these four polymer BHJ systems have dramatically smaller ΔG values, in agreement with their reduced backbone coplanarity and larger *d*-spacings. Further analysis of charge transport and recombination dynamics was carried out from the TRMC transients, which can be fit to an exponential decay function (Table 4). These resulting decay time constants, k_{rec}'s, correspond to long carrier recombination lifetimes.

Table 4. Summary of TRMC Results for PTPDnT and PBTInT BHJ Blend Films

Polymer	k_{rec} (μs)	ΔG_{max} (Relative)[a]	Polymer	k_{rec} (μs)	ΔG_{max} (Relative)[a]
PTPD1T	−	0.011	**PBTI1T**	−	0.043
PTPD2T	276	0.11	**PBTI2T**	80	0.20
PTPD3T	316	1.00	**PBTI3T**	142	0.80
PTPD3T′	9	0.060	**PBTI3T′**	−	0.095
PTPD3T″	−	0.030	**PBTI3T″**	−	0.045
PTPD4T	380	0.19	**PBTI4T**	177	0.90

[a]ΔG_{max} values are reported as relative to the highest value, **PTPD3T**.

Thus, for both **TPD** and **BTI** series, the carrier lifetime increases with increasing thiophene catenation, in good aggreement with their increased crystallinities. When comparing the **TPD** and **BTI** series, the fact that the **TPD** polymers generally exhibit slower decay dynamics further strengthens the observations made above about the higher degrees of crystalline properties, which is ideal for efficient charge transport. Finally comparing the decay dynamics of the **3T** derivatives reveals that the four polymers based on **3T′** and **3T″** all show far more rapid decay dynamics, suggesting facile carrier recombination, and are consistent with the poor PSC performance metrics, especially the significantly lower *FF*s and J_{sc}'s.

■ CONCLUSIONS

Two in-chain donor−acceptor copolymer series containing a variable-catenation oligothiophene donor and **TPD** or **BTI** acceptor blocks are synthesized and characterized. As a result of intramolecular S···O interactions, the **TPD**-based polymers show higher degrees of backbone coplanary and enhanced crystallinity versus the **BTI**-based analogues. By systematically increasing the thiophene number from **1T** to **4T**, the **PTPDnT** and **PBTInT** conjugation lengths are found to scale with **nT** catenation up to $n = 3$ and then saturate for longer oligomers. The oligothiophene catenation affords HOMO tunability from −5.67 to −5.23 eV for the **PTPDnT** series and −5.72 to −5.25 eV for the **PBTInT** series. The **TPD**-based polymers exhibit higher TFT mobilities than the corresponding **BTI** analogues owing to the higher degree of backbone coplanary and greater materials crystallinity, with polymers incorporating the **3T** unit having the highest mobilities in their respective series. In BHJ PSC blends with $PC_{71}BM$, optimal PCEs of 7.7% with exceptional *FF*s of 80% and 76% were achieved from **3T** polymers **PTPD3T** and **PBTI3T** in their series, respectively. Polymers employing **2T**, **3T**, and **4T** yield V_{oc}'s in the range of 0.65−0.95 V, reflecting their systematic HOMO variation. The results demonstrate that **3T** is the optimal donor unit among **nT**s ($n = 1$−4) for photovoltaic polymers. For the terthiophene-based polymers, subtle changes of alkylation patterns dramatically affect film morphology and PSC performance, and **PTPD3T′**, **PTPD3T″**, **PBTI3T′**, and **PBTI3T″** show much lower PCEs than **PTPD3T** and **PBTI3T**. By systematically varying donor polymer structural parameters, these results demonstrate the significance of simultaneously optimizing thiophene catenation along with the appropriate alkylation pattern in oligothiophene-based PSC materials.

Through a systematic structure−physical properties investigation using a range of diverse and complementary characterization methods, both macroscopic and microscopic characteristics of polymer:fullerene blend films are shown to be strongly dependent on polymer backbone geometry and the thiophene ring catenation. Specifically, increasing the thiophene number leads to enhanced polymer crystallinity. Comparing lamellar stacking distances of neat and blend films reveals that the **TPD** polymers, which preserve their crystalline phases without significant fullerene intercalation in polymer side chains, promote high local mobilities and longer carrier lifetimes. Although other factors such as domain connectivity, phase separations in both horizontal and vertical directions, electrode contact effects, and polymer orientations can also influence PSC performance and especially *FF*, the present findings argue that preserving highly crystalline polymer phases in the active blend films play an essential role in minimizing bimolecular recombination and enhancing *FF*s. The optimal performance of **PTPD3T** and **PBTI3T** BHJ blends can be attributed to their unique combination of optimal π-conjugation, close interpolymer interactions, long-range order, high charge carrier mobility, and optimal phase gradation. The results obtained in this work provide fundamental materials structure−device performance correlations and strongly suggest guidelines for designing oligothiophene-based polymers with optimal thiophene ring catenation and appropriate side chain substitution for maximizing PSC performance.

■ ASSOCIATED CONTENT

Ⓢ Supporting Information

The Supporting Information is available free of charge on the ACS Publications website at DOI: 10.1021/jacs.5b06462.

> Experimental and methods, including detailed synthesis and characterization of monomers and polymers, details of PSC and OTFT fabrication and characterization, OTFT and SCLC mobility measurements, theoretical calculations, and TRMC measurements. UV absorption of polymer solution, *J−V* characteristics of PSCs, and film morphologies (PDF)

■ AUTHOR INFORMATION

Corresponding Authors
*guoxg@sustc.edu.cn
*rocioponce@uma.es
*m-wasielewski@northwestern.edu
*lchen@anl.gov
*r-chang@northwetsern.edu
*a-facchetti@northwestern.edu
*t-marks@northwestern.edu

Notes
The authors declare no competing financial interest.

■ REFERENCES

(1) Krebs, F. C.; Jørgensen, M.; Norrman, K.; Hagemann, O.; Alstrup, J.; Nielsen, T. D.; Fyenbo, J.; Larsen, K.; Kristensen, J. *Sol. Energy Mater. Sol. Cells* **2009**, *93*, 422.
(2) Krebs, F. C. *Sol. Energy Mater. Sol. Cells* **2009**, *93*, 465.
(3) Scharber, M. C.; Sariciftci, N. S. *Prog. Polym. Sci.* **2013**, *38*, 1929.
(4) Gunes, S.; Neugebauer, H.; Sariciftci, N. S. *Chem. Rev.* **2007**, *107*, 1324.

(5) Ma, W.; Yang, C.; Gong, X.; Lee, K.; Heeger, A. J. *Adv. Funct. Mater.* **2005**, *15*, 1617.

(6) Cabanetos, C.; El Labban, A.; Bartelt, J. A.; Douglas, J. D.; Mateker, W. R.; Fréchet, J. M. J.; McGehee, M. D.; Beaujuge, P. M. *J. Am. Chem. Soc.* **2013**, *135*, 4656.

(7) Li, W.; Roelofs, W. S. C.; Wienk, M. M.; Janssen, R. A. J. *J. Am. Chem. Soc.* **2012**, *134*, 13787.

(8) Osaka, I.; Kakara, T.; Takemura, N.; Koganezawa, T.; Takimiya, K. *J. Am. Chem. Soc.* **2013**, *135*, 8834.

(9) He, Z.; Zhong, C.; Su, S.; Xu, M.; Wu, H.; Cao, Y. *Nat. Photonics* **2012**, *6*, 593.

(10) Liu, S.; Zhang, K.; Lu, J.; Zhang, J.; Yip, H.-L.; Huang, F.; Cao, Y. *J. Am. Chem. Soc.* **2013**, *135*, 15326.

(11) Chen, Z.; Cai, P.; Chen, J.; Liu, X.; Zhang, L.; Lan, L.; Peng, J.; Ma, Y.; Cao, Y. *Adv. Mater.* **2014**, *26*, 2586.

(12) Blouin, N.; Michaud, A.; Gendron, D.; Wakim, S.; Blair, E.; Neagu-Plesu, R.; Belletête, M.; Durocher, G.; Tao, Y.; Leclerc, M. *J. Am. Chem. Soc.* **2008**, *130*, 732.

(13) Warnan, J.; El Labban, A.; Cabanetos, C.; Hoke, E. T.; Shukla, P. K.; Risko, C.; Brédas, J.-L.; McGehee, M. D.; Beaujuge, P. M. *Chem. Mater.* **2014**, *26*, 2299.

(14) Zheng, Q.; Jung, B. J.; Sun, J.; Katz, H. E. *J. Am. Chem. Soc.* **2010**, *132*, 5394.

(15) Albrecht, S.; Janietz, S.; Schindler, W.; Frisch, J.; Kurpiers, J.; Kniepert, J.; Inal, S.; Pingel, P.; Fostiropoulos, K.; Koch, N.; Neher, D. *J. Am. Chem. Soc.* **2012**, *134*, 14932.

(16) Thompson, B. C.; Fréchet, J. M. J. *Angew. Chem., Int. Ed.* **2008**, *47*, 58.

(17) Dennler, G.; Scharber, M. C.; Ameri, T.; Denk, P.; Forberich, K.; Waldauf, C.; Brabec, C. J. *Adv. Mater.* **2008**, *20*, 579.

(18) Hendriks, K. H.; Li, W.; Wienk, M. M.; Janssen, R. A. J. *J. Am. Chem. Soc.* **2014**, *136*, 12130.

(19) Roncali, J. *Chem. Rev.* **1997**, *97*, 173.

(20) Gendron, D.; Leclerc, M. *Energy Environ. Sci.* **2011**, *4*, 1225.

(21) Liang, Y.; Yu, L. *Acc. Chem. Res.* **2010**, *43*, 1227.

(22) Ye, L.; Zhang, S.; Huo, L.; Zhang, M.; Hou, J. *Acc. Chem. Res.* **2014**, *47*, 1595.

(23) Guo, X.; Facchetti, A.; Marks, T. J. *Chem. Rev.* **2014**, *114*, 8943.

(24) Kroon, R.; Diaz de Zerio Mendaza, A.; Himmelberger, S.; Bergqvist, J.; Bäcke, O.; Faria, G. C.; Gao, F.; Obaid, A.; Zhuang, W.; Gedefaw, D.; Olsson, E.; Inganäs, O.; Salleo, A.; Müller, C.; Andersson, M. R. *J. Am. Chem. Soc.* **2014**, *136*, 11578.

(25) Stalder, R.; Mei, J.; Graham, K. R.; Estrada, L. A.; Reynolds, J. R. *Chem. Mater.* **2014**, *26*, 664.

(26) Guo, X.; Zhou, N.; Lou, S. J.; Hennek, J. W.; Ponce Ortiz, R.; Butler, M. R.; Boudreault, P.-L. T.; Strzalka, J.; Morin, P.-O.; Leclerc, M.; López Navarrete, J. T.; Ratner, M. A.; Chen, L. X.; Chang, R. P. H.; Facchetti, A.; Marks, T. J. *J. Am. Chem. Soc.* **2012**, *134*, 18427.

(27) Carsten, B.; He, F.; Son, H. J.; Xu, T.; Yu, L. *Chem. Rev.* **2011**, *111*, 1493.

(28) Piliego, C.; Holcombe, T. W.; Douglas, J. D.; Woo, C. H.; Beaujuge, P. M.; Fréchet, J. M. J. *J. Am. Chem. Soc.* **2010**, *132*, 7595.

(29) Oberhumer, P. M.; Huang, Y.-S.; Massip, S.; James, D. T.; Tu, G.; Albert-Seifried, S.; Beljonne, D.; Cornil, J.; Kim, J.-S.; Huck, W. T. S.; Greenham, N. C.; Hodgkiss, J. M.; Friend, R. H. *J. Chem. Phys.* **2011**, *134*, 114901.

(30) Zhou, N.; Guo, X.; Ortiz, R. P.; Li, S.; Zhang, S.; Chang, R. P. H.; Facchetti, A.; Marks, T. J. *Adv. Mater.* **2012**, *24*, 2242.

(31) Guo, X.; Ortiz, R. P.; Zheng, Y.; Hu, Y.; Noh, Y.-Y.; Baeg, K.-J.; Facchetti, A.; Marks, T. J. *J. Am. Chem. Soc.* **2011**, *133*, 1405.

(32) Amb, C. M.; Chen, S.; Graham, K. R.; Subbiah, J.; Small, C. E.; So, F.; Reynolds, J. R. *J. Am. Chem. Soc.* **2011**, *133*, 10062.

(33) Wu, Q.; Wang, M.; Qiao, X.; Xiong, Y.; Huang, Y.; Gao, X.; Li, H. *Macromolecules* **2013**, *46*, 3887.

(34) Small, C. E.; Chen, S.; Subbiah, J.; Amb, C. M.; Tsang, S.-W.; Lai, T.-H.; Reynolds, J. R.; So, F. *Nat. Photonics* **2012**, *6*, 115.

(35) Guo, X.; Zhou, N.; Lou, S. J.; Smith, J.; Tice, D. B.; Hennek, J. W.; Ortiz, R. P.; Navarrete, J. T. L.; Li, S.; Strzalka, J.; Chen, L. X.; Chang, R. P. H.; Facchetti, A.; Marks, T. J. *Nat. Photonics* **2013**, *7*, 825.

(36) Wu, Z.; Yang, T.; Ong, B. S.; Liang, Y.; Guo, X. *Org. Photon. Photovolt.* **2014**, *2*, 21.

(37) Chu, T.-Y.; Lu, J.; Beaupré, S.; Zhang, Y.; Pouliot, J.-R.; Wakim, S.; Zhou, J.; Leclerc, M.; Li, Z.; Ding, J.; Tao, Y. *J. Am. Chem. Soc.* **2011**, *133*, 4250.

(38) Li, W.; Albrecht, S.; Yang, L.; Roland, S.; Tumbleston, J. R.; McAfee, T.; Yan, L.; Kelly, M. A.; Ade, H.; Neher, D.; You, W. *J. Am. Chem. Soc.* **2014**, *136*, 15566.

(39) Ong, B. S.; Wu, Y.; Liu, P.; Gardner, S. *J. Am. Chem. Soc.* **2004**, *126*, 3378.

(40) McCulloch, I.; Heeney, M.; Bailey, C.; Genevicius, K.; MacDonald, I.; Shkunov, M.; Sparrowe, D.; Tierney, S.; Wagner, R.; Zhang, W.; Chabinyc, M. L.; Kline, R. J.; McGehee, M. D.; Toney, M. F. *Nat. Mater.* **2006**, *5*, 328.

(41) Ko, S.; Verploegen, E.; Hong, S.; Mondal, R.; Hoke, E. T.; Toney, M. F.; McGehee, M. D.; Bao, Z. *J. Am. Chem. Soc.* **2011**, *133*, 16722.

(42) Li, W.; Hendriks, K. H.; Roelofs, W. S. C.; Kim, Y.; Wienk, M. M.; Janssen, R. A. J. *Adv. Mater.* **2013**, *25*, 3182.

(43) Guo, X.; Cui, C.; Zhang, M.; Huo, L.; Huang, Y.; Hou, J.; Li, Y. *Energy Environ. Sci.* **2012**, *5*, 7943.

(44) Vohra, V.; Kawashima, K.; Kakara, T.; Koganezawa, T.; Osaka, I.; Takimiya, K.; Murata, H. *Nat. Photonics* **2015**, *9*, 403.

(45) Liu, Y.; Zhao, J.; Li, Z.; Mu, C.; Ma, W.; Hu, H.; Jiang, K.; Lin, H.; Ade, H.; Yan, H. *Nat. Commun.* **2014**, *5*, 5293.

(46) Kan, B.; Li, M.; Zhang, Q.; Liu, F.; Wan, X.; Wang, Y.; Ni, W.; Long, G.; Yang, X.; Feng, H.; Zuo, Y.; Zhang, M.; Huang, F.; Cao, Y.; Russell, T. P.; Chen, Y. *J. Am. Chem. Soc.* **2015**, *137*, 3886.

(47) Kan, B.; Zhang, Q.; Li, M.; Wan, X.; Ni, W.; Long, G.; Wang, Y.; Yang, X.; Feng, H.; Chen, Y. *J. Am. Chem. Soc.* **2014**, *136*, 15529.

(48) Sun, K.; Xiao, Z.; Lu, S.; Zajaczkowski, W.; Pisula, W.; Hanssen, E.; White, J. M.; Williamson, R. M.; Subbiah, J.; Ouyang, J.; Holmes, A. B.; Wong, W. W. H.; Jones, D. J. *Nat. Commun.* **2015**, *6*, 6013.

(49) Servaites, J. D.; Ratner, M. A.; Marks, T. J. *Energy Environ. Sci.* **2011**, *4*, 4410.

(50) Noriega, R.; Rivnay, J.; Vandewal, K.; Koch, F. P. V.; Stingelin, N.; Smith, P.; Toney, M. F.; Salleo, A. *Nat. Mater.* **2013**, *12*, 1038.

(51) Huang, Y.; Kramer, E. J.; Heeger, A. J.; Bazan, G. C. *Chem. Rev.* **2014**, *114*, 7006.

(52) Graham, K. R.; Cabanetos, C.; Jahnke, J. P.; Idso, M. N.; El Labban, A.; Ngongang Ndjawa, G. O.; Heumueller, T.; Vandewal, K.; Salleo, A.; Chmelka, B. F.; Amassian, A.; Beaujuge, P. M.; McGehee, M. D. *J. Am. Chem. Soc.* **2014**, *136*, 9608.

(53) Szarko, J. M.; Rolczynski, B. S.; Lou, S. J.; Xu, T.; Strzalka, J.; Marks, T. J.; Yu, L.; Chen, L. X. *Adv. Funct. Mater.* **2014**, *24*, 10.

(54) Jackson, N. E.; Savoie, B. M.; Kohlstedt, K. L.; Olvera de la Cruz, M.; Schatz, G. C.; Chen, L. X.; Ratner, M. A. *J. Am. Chem. Soc.* **2013**, *135*, 10475.

(55) Rolczynski, B. S.; Szarko, J. M.; Son, H. J.; Yu, L.; Chen, L. X. *J. Phys. Chem. Lett.* **2014**, *5*, 1856.

(56) Su, M.-S.; Kuo, C.-Y.; Yuan, M.-C.; Jeng, U. S.; Su, C.-J.; Wei, K.-H. *Adv. Mater.* **2011**, *23*, 3315.

(57) Jo, J.; Pron, A.; Berrouard, P.; Leong, W. L.; Yuen, J. D.; Moon, J. S.; Leclerc, M.; Heeger, A. J. *Adv. Energy Mater.* **2012**, *2*, 1397.

(58) Li, Y.; Sonar, P.; Murphy, L.; Hong, W. *Energy Environ. Sci.* **2013**, *6*, 1684.

(59) Ma, Z.; Sun, W.; Himmelberger, S.; Vandewal, K.; Tang, Z.; Bergqvist, J.; Salleo, A.; Andreasen, J. W.; Inganas, O.; Andersson, M. R.; Muller, C.; Zhang, F.; Wang, E. *Energy Environ. Sci.* **2014**, *7*, 361.

(60) Fu, B.; Baltazar, J.; Hu, Z.; Chien, A.-T.; Kumar, S.; Henderson, C. L.; Collard, D. M.; Reichmanis, E. *Chem. Mater.* **2012**, *24*, 4123.

(61) Fei, Z.; Pattanasattayavong, P.; Han, Y.; Schroeder, B. C.; Yan, F.; Kline, R. J.; Anthopoulos, T. D.; Heeney, M. *J. Am. Chem. Soc.* **2014**, *136*, 15154.

(62) Pomerantz, M. *Tetrahedron Lett.* **2003**, *44*, 1563.

(63) Hutchison, G. R.; Ratner, M. A.; Marks, T. J. *J. Am. Chem. Soc.* **2005**, *127*, 16866.

(64) Guo, X.; Ortiz, R. P.; Zheng, Y.; Kim, M.-G.; Zhang, S.; Hu, Y.; Lu, G.; Facchetti, A.; Marks, T. J. *J. Am. Chem. Soc.* **2011**, *133*, 13685.

(65) Castiglioni, C.; Lopez Navarrete, J. T.; Zerbi, G.; Gussoni, M. *Solid State Commun.* **1988**, *65*, 625.

(66) Ponce Ortiz, R.; Casado, J.; Hernández, V.; López Navarrete, J. T.; Viruela, P. M.; Ortí, E.; Takimiya, K.; Otsubo, T. *Angew. Chem., Int. Ed.* **2007**, *46*, 9057.

(67) Ponce Ortiz, R.; Herrera, H.; Mancheño, M. J.; Seoane, C.; Segura, J. L.; Mayorga Burrezo, P.; Casado, J.; López Navarrete, J. T.; Facchetti, A.; Marks, T. J. *Chem. - Eur. J.* **2013**, *19*, 12458.

(68) Ferrón, C. C.; Sheynin, Y.; Li, M.; Patra, A.; Bendikov, M.; López Navarrete, J. T.; Hernández, V.; Ruiz Delgado, M. C. *Isr. J. Chem.* **2014**, *54*, 759.

(69) Hernandez, V.; Castiglioni, C.; Del Zoppo, M.; Zerbi, G. *Phys. Rev. B: Condens. Matter Mater. Phys.* **1994**, *50*, 9815.

(70) Hernández, V.; Casado, J.; Ramírez, F. J.; Zotti, G.; Hotta, S.; López Navarrete, J. T. *J. Chem. Phys.* **1996**, *104*, 9271.

(71) Oberhumer, P. M.; Huang, Y.-S.; Massip, S.; James, D. T.; Tu, G.; Albert-Seifried, S.; Beljonne, D.; Cornil, J.; Kim, J.-S.; Huck, W. T. S.; Greenham, N. C.; Hodgkiss, J. M.; Friend, R. H. *J. Chem. Phys.* **2011**, *134*, 114901.

(72) Ko, S.; Hoke, E. T.; Pandey, L.; Hong, S.; Mondal, R.; Risko, C.; Yi, Y.; Noriega, R.; McGehee, M. D.; Brédas, J.-L.; Salleo, A.; Bao, Z. *J. Am. Chem. Soc.* **2012**, *134*, 5222.

(73) Faist, M. A.; Shoaee, S.; Tuladhar, S.; Dibb, G. F. A.; Foster, S.; Gong, W.; Kirchartz, T.; Bradley, D. D. C.; Durrant, J. R.; Nelson, J. *Adv. Energy Mater.* **2013**, *3*, 744.

(74) Azimi, H.; Senes, A.; Scharber, M. C.; Hingerl, K.; Brabec, C. J. *Adv. Energy Mater.* **2011**, *1*, 1162.

(75) Lee, J. K.; Ma, W. L.; Brabec, C. J.; Yuen, J.; Moon, J. S.; Kim, J. Y.; Lee, K.; Bazan, G. C.; Heeger, A. J. *J. Am. Chem. Soc.* **2008**, *130*, 3619.

(76) Sun, Y.; Welch, G. C.; Leong, W. L.; Takacs, C. J.; Bazan, G. C.; Heeger, A. J. *Nat. Mater.* **2012**, *11*, 44.

(77) Lou, S. J.; Szarko, J. M.; Xu, T.; Yu, L.; Marks, T. J.; Chen, L. X. *J. Am. Chem. Soc.* **2011**, *133*, 20661.

(78) Scharber, M. C.; Mühlbacher, D.; Koppe, M.; Denk, P.; Waldauf, C.; Heeger, A. J.; Brabec, C. J. *Adv. Mater.* **2006**, *18*, 789.

(79) Dimitrov, S. D.; Bakulin, A. A.; Nielsen, C. B.; Schroeder, B. C.; Du, J.; Bronstein, H.; McCulloch, I.; Friend, R. H.; Durrant, J. R. *J. Am. Chem. Soc.* **2012**, *134*, 18189.

(80) Hörmann, U.; Lorch, C.; Hinderhofer, A.; Gerlach, A.; Gruber, M.; Kraus, J.; Sykora, B.; Grob, S.; Linderl, T.; Wilke, A.; Opitz, A.; Hansson, R.; Anselmo, A. S.; Ozawa, Y.; Nakayama, Y.; Ishii, H.; Koch, N.; Moons, E.; Schreiber, F.; Brütting, W. *J. Phys. Chem. C* **2014**, *118*, 26462.

(81) Kyaw, A. K. K.; Wang, D. H.; Gupta, V.; Leong, W. L.; Ke, L.; Bazan, G. C.; Heeger, A. J. *ACS Nano* **2013**, *7*, 4569.

(82) Warnan, J.; Cabanetos, C.; Bude, R.; El Labban, A.; Li, L.; Beaujuge, P. M. *Chem. Mater.* **2014**, *26*, 2829.

(83) Miller, N. C.; Sweetnam, S.; Hoke, E. T.; Gysel, R.; Miller, C. E.; Bartelt, J. A.; Xie, X.; Toney, M. F.; McGehee, M. D. *Nano Lett.* **2012**, *12*, 1566.

(84) Smilgies, D.-M. *J. Appl. Crystallogr.* **2009**, *42*, 1030.

(85) Cates, N. C.; Gysel, R.; Beiley, Z.; Miller, C. E.; Toney, M. F.; Heeney, M.; McCulloch, I.; McGehee, M. D. *Nano Lett.* **2009**, *9*, 4153.

(86) Sweetnam, S.; Graham, K. R.; Ngongang Ndjawa, G. O.; Heumüller, T.; Bartelt, J. A.; Burke, T. M.; Li, W.; You, W.; Amassian, A.; McGehee, M. D. *J. Am. Chem. Soc.* **2014**, *136*, 14078.

(87) Zusan, A.; Vandewal, K.; Allendorf, B.; Hansen, N. H.; Pflaum, J.; Salleo, A.; Dyakonov, V.; Deibel, C. *Adv. Energy Mater.* **2014**, *4*, 1400922.

(88) Stuart, A. C.; Tumbleston, J. R.; Zhou, H.; Li, W.; Liu, S.; Ade, H.; You, W. *J. Am. Chem. Soc.* **2013**, *135*, 1806.

(89) Infelta, P. P.; de Haas, M. P.; Warman, J. M. *Radiat. Phys. Chem.* **1977**, *10*, 353.

(90) Saeki, A.; Tsuji, M.; Seki, S. *Adv. Energy Mater.* **2011**, *1*, 661.

(91) Ferguson, A. J.; Kopidakis, N.; Shaheen, S. E.; Rumbles, G. *J. Phys. Chem. C* **2011**, *115*, 23134.

(92) Nardes, A. M.; Ayzner, A. L.; Hammond, S. R.; Ferguson, A. J.; Schwartz, B. J.; Kopidakis, N. *J. Phys. Chem. C* **2012**, *116*, 7293.

(93) Coffey, D. C.; Larson, B. W.; Hains, A. W.; Whitaker, J. B.; Kopidakis, N.; Boltalina, O. V.; Strauss, S. H.; Rumbles, G. *J. Phys. Chem. C* **2012**, *116*, 8916.

(94) Saeki, A.; Yoshikawa, S.; Tsuji, M.; Koizumi, Y.; Ide, M.; Vijayakumar, C.; Seki, S. *J. Am. Chem. Soc.* **2012**, *134*, 19035.

(95) De Haas, M. P.; Warman, J. M. *Chem. Phys.* **1982**, *73*, 35.

(96) Laiho, R.; Poloskin, D. S.; Stepanov, Y. P.; Vlasenko, M. P.; Vlasenko, L. S.; Zakhvalinskii, V. S. *J. Appl. Phys.* **2009**, *106*, 013712.

(97) Savenije, T.; Kroeze, J.; Wienk, M.; Kroon, J.; Warman, J. *Phys. Rev. B: Condens. Matter Mater. Phys.* **2004**, *69*, 155205.

(98) Dicker, G.; de Haas, M.; Siebbeles, L.; Warman, J. *Phys. Rev. B: Condens. Matter Mater. Phys.* **2004**, *70*, 045203.

(99) Nardes, A. M.; Ferguson, A. J.; Whitaker, J. B.; Larson, B. W.; Larsen, R. E.; Maturová, K.; Graf, P. A.; Boltalina, O. V.; Strauss, S. H.; Kopidakis, N. *Adv. Funct. Mater.* **2012**, *22*, 4115.